

IN-02
086725

Improved Models For The Porous Surface With Passive Control

Sandra L. Kraushaar and Ndaona Chokani
North Carolina State University, Raleigh, North Carolina

NASA Langley Research Center Grant NAG-1-1819. (Final)

Abstract

A computational investigation of afterbody flow using a passive control method is conducted. The passive control method consists of a porous surface placed over a plenum. The purpose of the passive control method is to exploit the adverse pressure gradient present in afterbody flow in an attempt to reduce boundary layer separation and afterbody drag. Four different porous wall models are used to model the transpiration velocity in the region of passive control. A three-dimensional, time-dependent, Reynolds-averaged, simplified Navier-Stokes solver, *PAB3D*, is used to simulate afterbody flow with and without passive control. Three afterbody configurations with boat-tail angles of 10° , 20° and 30° are used to obtain two-dimensional solutions with a freestream Mach number of 0.6 and nozzle pressure ratio of 6. The region of passive control was initially placed from 20%-60% of the nozzle length. The effect of the porous placement and porous extent is also studied. Baseline (no porosity) two-dimensional solutions are qualitatively similar to experimental data but under-predict the magnitude of the pressure recovery. Results for the subsonic solutions show losses in the pressure recovery for some cases with passive control. Three-dimensional effects are also investigated and seen to be very significant. Three-dimensional baseline solutions, for both sub- and **super**-critical freestream Mach numbers, compare very favorably with the experimental data in comparison to the two-dimensional solution. Future work is required to examine three-dimensional afterbody flows with passive porosity.

Acknowledgements

This work was first presented as the MS thesis of the first author at North Carolina State University. The second author served as academic advisor during the course of the first author's graduate studies.

The authors thank Paul S. Pao, Karen A. Deere, and John R. Carlson of NASA Langley Research Center (LaRC) for their input regarding the Navier-Stokes solver and grid generation code. The authors would also like to extend thanks to Linda S. Bangert and Steven X. S. Bauer of NASA LaRC for their support in project formulation and the funding under NASA LaRC grant NAG-1-1819.

Nomenclature

C	permeability factor
C_d	discharge coefficient, w_p/w_i
C_p	coefficient of pressure, $(p-p_\infty)/q_\infty$
C_{pc}	characteristic specific heat
E, F, G	flux vectors in x, y, z directions, respectively
F_A	axial thrust, N
F_i	ideal isentropic thrust, N
	flux vector in η direction
H	ratio of hole depth to plate thickness
J	Jacobian of coordinate transformation
M	Mach number
NPR	nozzle pressure ratio, $p_{t,j}/p_\infty$
P	ratio of hole area to total area (porosity fraction)
Pr	Prandtl Number
\underline{Q}	vector of conserved quantities
T	temperature, K
d	diameter of porous holes, m
d_h	hydraulic diameter of porous holes, m
e	total energy
k	heat transfer coefficient
p	local static pressure, Pa
$p_{t,j}$	jet total pressure, Pa
q	dynamic pressure, Pa
t	time
t_h	thickness of porous plate, m
u, v, w	velocity component in x, y, z directions, respectively
v_w	transpiration velocity (normal to surface), m/s
w_i	ideal mass flow rate, kg/s
w_p	mass flow rate, kg/s
x	coordinate in streamwise direction
x_f	finish location of the porous region, m
x_s	start location of the porous region, m
y	coordinate in spanwise direction
z	coordinate in vertical direction
γ	ratio of specific heats
ζ	generalized coordinate in radial direction
η	generalized coordinate in circumferential direction
μ	molecular viscosity, $kg/m-s$
ξ	generalized coordinate in streamwise direction
ρ	density, kg/m^3

τ	shear stress
$l11$	fine grid sequence
$l22$	medium grid sequence
$l44$	coarse grid sequence

Subscripts

∞	freestream condition
p	plenum condition
t	partial derivative with respect to time
v	viscous condition
w	wall condition
x, y, z	partial derivative with respect to corresponding Cartesian coordinate
ξ, η, ζ	partial derivative with respect to corresponding generalized coordinate

Superscripts

L	laminar condition
T	turbulent condition

1. Introduction

The flow past an airfoil or afterbody can contribute greatly to the drag of an aircraft, and thus, is of concern in the fields of military and civil aviation. Such drag may increase significantly in the presence of flow separation. In subsonic flows, separation may occur if the attached flow is unable to negotiate the adverse pressure gradient imposed by the geometry of the airfoil or afterbody. In transonic flows, the presence of a shockwave is an additional mechanism that can induce flow separation. Flow separation causes viscous dissipation and a large increase in the form drag. It is the objective of boundary layer control to eliminate or minimize the flow separation, and thus decrease drag. This ultimately improves the aerodynamic efficiency of airfoils and the aeropropulsive efficiency of after-bodies. In the present work, we are concerned with boundary layer control on aircraft after-bodies.

Methods of boundary layer control may be classified as either active or passive control methods. Active control methods employ either suction from, or blowing into, the boundary layer to eliminate or minimize flow separation. With the use of suction, low momentum fluid close to the wall is removed, and the remaining higher momentum fluid is better able to withstand the adverse pressure gradient without separating. The addition of high momentum fluid adjacent the wall is accomplished through boundary layer blowing. The added fluid increases mixing in the boundary layer and thus, minimizes flow separation. Active control methods, however, have some penalties. The auxiliary equipment, including pumps, valves, and meters, result in added weight, complexity, and costs which may outweigh the benefits of the drag reduction.

Passive control methods, in contrast, are simpler, have a lower cost of implementation, and no additional weight. Passive control exploits naturally occurring phenomena to obtain desirable flow

characteristics. The passive control method examined in this investigation is that of passive porosity. As shown in Figure 1, this control approach uses a porous surface placed above a plenum in a region with large pressure gradients; in this example, the pressure gradients are a result of a shockwave. The high-pressure region over the aft portion of the porous surface is allowed to communicate with the low-pressure region over the forward portion of the porous surface. This communication through the porous region produces suction over the aft portion and blowing over the forward portion. The natural suction over the aft portion of the porous surface decreases the boundary layer thickness and increases the skin friction. Blowing on the forward portion of the porous surface increases the boundary layer thickness and decreases the skin friction. The coupled suction and blowing provided by this passive control method can yield the benefits of both suction and blowing – reduced pressure gradient and prevention of flow separation – without the added cost and space associated with the active control approaches.

Several experimental studies have examined the effect of passive porosity. Previous research has shown that the method of passive porosity can enhance wing performance at transonic speeds by reducing or eliminating shock-induced separation. Bahi^{1,2} conducted experimental tests to examine the effect of passive porosity on circular arc and supercritical airfoils. The experiments showed that the shock structure was modified from a normal shock without porosity to a lambda shock with passive porosity. The flow through the porous surface, blowing upstream and suction downstream of the shockwave, minimized the flow separation. Raghunathan and Mabey conducted similar tests on a circular arc airfoil³. Their experimental tests included not only holes normal to the surface of the airfoil in the porous region, but forward- and backward-facing holes as well. Pressure profiles in the wake confirmed increases in viscous losses near the wall, and an overall drag reduction was seen for all hole configurations. Experiments conducted on ogive-forebodies by

Bauer et al⁴ showed that passive porosity reduces the side force at subsonic and transonic speeds. These studies¹⁻⁴ suggest that there is also potential to reduce aircraft afterbody drag through the application of passive porosity.

Several researchers have employed computational methods in examining the passive porosity control method. The inclusion, however, of the plenum and individual holes associated with the passive porosity geometry in the computational domain can be complicated and expensive. Thus, boundary conditions modeling the flow in the porous region have been investigated to reduce the size and cost of computations with passive porosity. Chokani and Squire⁵ computationally modeled a passive porosity wind tunnel experiment. A linear Darcy pressure law was used with a constant porosity coefficient to model the transpiration velocity in the porous region. Under the assumption of the Darcy law that the pressure change is the only driving force in the calculation of the transpiration velocity, agreement was reasonable compared to the experimental results. Hanna⁶ examined the use of passive porosity in hypersonic shockwave/turbulent boundary layer interactions with the same Darcy pressure law as used in Ref. 5. However, in Ref 6, a variable (sinusoidal in nature) porosity coefficient was also used. The variable porosity coefficient predicted differences in the transpiration velocity in the interaction region but similar pressure distribution when compared to results using a constant porosity coefficient.

The inadequacies in the above models arise in their simplicity. The assumed linear relationship between the transpiration velocity and the pressure change across the porous plate does not adequately represent the actual flow physics. Other factors such as plenum and hole geometry have been shown to affect flow characteristics in the porous region². There also exists no constitutive relation between the porosity coefficient used in the Darcy law and actual geometry of the porous material. Hence, this study examines more physically based models⁷ for the porous surface with

passive control. The application of these models to the flow over an aircraft afterbody is also examined.

The approach in this work is computational in nature. A Navier-Stokes code, *PAB3D*, is used to simulate the afterbody flow with and without passive porosity. The code is modified to examine the adequacy of different porous wall models. The specific objectives of this study are:

- i) to evaluate porous wall models for passive porosity; and
- ii) to computationally examine the effectiveness of afterbody flow control using passive porosity.

The numerical procedure is outlined in the following chapter; the details of the different porous wall models are described. In the next chapter, the results of this study are then described; these results include the validation of the porosity models and both two- and three-dimensional computational solutions of afterbody flows. The last chapter summarizes the significant findings of the study and suggests areas for future work.

2. Numerical Procedure

2.1 Governing Equations

The governing equations of interest in this study are the three-dimensional, time-dependent, Reynolds-averaged, simplified Navier-Stokes equations. These equations are described in full in Appendix A. As the dominant dissipative effects arise from diffusion normal to the surface of the afterbody model, only the diffusion terms normal to the surface are retained in the governing equations. This optional representation of the Navier-Stokes equations is commonly referred to as a thin layer approximation. In a generalized coordinate system, the resulting conservative form of the governing equations is expressed as

$$\hat{Q}_t + \hat{F}_{\xi} + \hat{G}_{\eta} + \hat{H}_{\zeta} = 0$$

where

$$\hat{G} = \frac{1}{J}(\eta_t Q + \eta_x F + \eta_y G + \eta_z H)$$

and other variables defined as outlined in Appendix A. The ideal gas relationships for energy, enthalpy and pressure complete the system of equations.

2.2 Computational Algorithm

The general three-dimensional Navier-Stokes code *PAB3D* was used to obtain solutions of the system of governing equations. The *PAB3D* code is more fully described elsewhere⁸⁻¹⁰, but a few important features are presented here. The code uses a finite volume formulation in which the spatial derivatives in the governing equations are evaluated as conservative flux balances across grid cells. The convective flux terms at the cell interfaces are determined with a Roe, upwind-biased, flux-difference scheme; the scheme is spatially third-order accurate. The van Leer scheme

is used to construct the implicit operator. Central differencing is used for the diffusion terms of the fluxes. An approximately factored, alternating-direction-implicit scheme in delta form is used for the time-differencing algorithm. A detailed description of the mathematical formulation for these schemes can be found in other literature⁸.

The numerical code has the option for either space- or time-marching solutions. The space-marching option is well suited for supersonic flows or flows in which pressure gradients are practically absent. When space-marching criterion were met, the space-marching algorithm was used as the computer time required for the space-marched solution is significantly less than that for the time-marched procedure. The code *PAB3D* has options for numerous algebraic Reynolds stress turbulence models to calculate of the turbulent shear stress^{12,13}. Linear k - ε equations are available which include the use of the damping function of Jones & Launder¹⁴. Non-linear algebraic Reynolds stress models are also available including those of Shih, Zhu & Lumley¹⁵ and Girimaji¹⁶. The use of a particular model will be noted later as it is applied. The initialization of the viscous flow transition from laminar to turbulent is done by the placement of k and ε profiles at user-specified lines or planes in the flowfield. This initial turbulent profile then develops as permitted by local flow conditions.

2.3 Boundary Conditions

The boundary conditions along the block faces were specified as follows. The Riemann invariants along characteristic lines were used to calculate the primitive flow variables at the freestream inflow boundary face and the lateral outer boundary faces. Symmetry boundary conditions were imposed along the centerlines upstream and downstream of a model and along the internal jet centerline. The internal nozzle inflow boundary face for the afterbody geometry was specified using total pressure and temperature. At the downstream boundary faces, an extrapolation

boundary condition is applied. No-slip, impermeable, adiabatic, zero normal pressure gradient boundary conditions were applied along all solid walls. For regions of passive control, no-slip, permeable, adiabatic, zero-normal pressure gradient boundary conditions were applied; four different porosity models were examined to determine the transpiration velocity in regions of passive control.

2.4 Porosity Models

2.4.1 Darcy-Constant Model

The plenum chamber below a porous surface is assumed closed except for the porous surface itself. Thus, the net mass flow rate over the porous surface is zero, i.e.

$$\int \rho_w v_w dx = 0$$

The first porosity model (Darcy-constant) is the linear form of the Darcy pressure-velocity law present in the original *PAD3D* code. The velocity normal to the wall is specified as

$$v_w = aC(p_p - p_w)$$

where

$$a = \frac{1}{\sqrt{\rho_w p_w}}$$

and $C=C_I$ is a user defined constant permeability factor. Assuming the plenum pressure is constant, the plenum pressure may be determined from

$$p_p = \frac{\int a \rho_w p_w dx}{\int a \rho_w dx}$$

A similar procedure is used in the determination of the plenum pressure for all the other porosity models.

2.4.2 Darcy-sinusoidal Model

The second model (Darcy-sinusoidal) follows Hanna⁶ where the Darcy law, is used with a sinusoidal varying permeability factor:

$$C = C_1 \left[\frac{1}{2} + \sqrt{\sin\left(\frac{\pi(x - x_s)}{x_f - x_s}\right)} \right]$$

where C_1 is the same permeability factor as used in the Darcy-constant model.

The widespread usage of the above two Darcy models in previous research is due in part to their simplicity. The assumption that the transpiration velocity is driven only by the change in pressure across the porous surface provides a model that is easy to implement in a computer code. The simplicity of the model, however, is the source of its limitations. The Darcy law poorly models flow physics as it assumes a linear relationship between the change in pressure and the transpiration velocity. The model also neglects potentially important parameters such as thickness of porous plate, hole diameter and length, and geometry of plenum. Also, the choice of permeability factor is at present arbitrary. A calibration of the permeability factor is required for accurate representation of a degree of porosity.

2.4.3 Darcy-geometric Model

Idel'cik⁷ has shown that the effects of porosity not only depend on the pressure change across the porous plate, but also the characteristics of the flow through the holes in the porous region and the hole geometry. The third model (Darcy-geometric) thus uses the Darcy law in the form:

$$v_w = \frac{r}{\mu_w t_h} (p_p - p_w)$$

where the permeability r is defined by

$$r = \frac{P d_h^2}{32 H^2}$$

where H is the ratio of hole depth to plate thickness. In cases presented here, the porous surface is considered flat with holes perpendicular to the plate surface, hence $H=1$. Also, cylindrical shaped holes are assumed in the porous region, and the hydraulic diameter is then the geometric diameter of the holes, i.e. $d_h=d$.

2.4.4 Pipe Flow Model

In the investigation by Poll and Danks¹⁷ the transpiration velocity in the porous region is determined by the assumption that the flow through each hole in the porous plate is “pipe” like. The pipe draws air from the high-pressure side of the porous plate, and ejects it in the form of a jet on the low-pressure side. The resulting non-linear relation is used as the fourth model (Pipe flow);

$$Y = 40.76X + 1.962X^2$$

where

$$X = \frac{\pi \rho_w d^2}{4 \mu_w t_h} v_w$$

$$Y = \frac{\rho_w d^4}{(\mu_w t_h)^2} (p_w - p_p) + \frac{1}{2} \left(\frac{\rho_w d^2}{\mu_w t_h} v_w \right)^2$$

As this model implicitly expresses the transpiration velocity as a function of the plenum pressure, a secant method of iteration is used to determine the plenum pressure.

2.5 Experimental Database

The experimental data used as baseline test cases were obtained by Carlson and Asbury¹⁸ in tests conducted in the NASA Langley Research Center's 16-Foot Transonic Wind Tunnel¹⁹. The test model was a three-dimensional isolated nacelle geometry with interchangeable after-bodies. Three nozzle boat-tail angles of 10°, 20° and 30° without passive control were tested over a range of Mach numbers and nozzle pressure ratios. An external high-pressure air system was used to simulate the internal flow and to exhaust a jet from the nozzle. Pressure taps were located externally on the centerline of the afterbody to obtain surface pressure distributions. A balance used with the model provided aerodynamic data such as drag.

2.6 Grid Generation

The algebraic grid generation code developed by Pao²⁰ was used to generate the body-fitted, structured, computational grids used in this study. A multiblock/multizone grid structure was employed allowing each of the six faces on a block to have any combination of boundary conditions. On wall bounded blocks, the initial cell height and grid stretching were examined to ensure that the grid was capable of resolving flow properties in a boundary layer. Cell size matching at block interfaces was also enforced to ensure good communications between blocks.

2.7 Performance Analysis

Nozzle performance characteristics were obtained through the use of a nozzle performance package developed by Carlson²¹. The aero-propulsive forces are determined through the application of the momentum theorem to a control volume surrounding the nozzle. That is, the

mass flux and pressure forces are integrated over the control volume to obtain the net force acting on the control volume:

$$\vec{F} = \sum \rho \vec{U} (\vec{U} \cdot \vec{n}) + (p - p_{\infty}) \vec{n} \nabla A + F_{fric}$$

where F is the total vector body force, ∇A is the area attributed to the cell face, and skin friction, F_{fric} is calculated along solid wall boundaries.

3. Results and Discussion

The porous wall models were first evaluated by examining two transonic shockwave/boundary layer interaction test cases, Chokani and Squire⁵ and Bahi^{1,2}. A grid refinement study was then conducted on the two-dimensional afterbody grid to assure solutions obtained would be grid independent. The effect of passive porosity on afterbody flow is first studied on the two-dimensional grid at subsonic freestream conditions. The effects of the placement of the porous region as well as its extent are also studied. Finally, the three-dimensional effects on the afterbody flow are investigated and compared to the two-dimensional solutions.

3.1 Validation Results

3.1.1 Passive Control on a Flat Plate

Chokani and Squire⁵ conducted an experimental and computational study of the passive porosity concept. The experimental set-up consisted of a circular arc airfoil of chord 80mm and radius of curvature 163mm placed on the floor of the wind tunnel. At a freestream Mach number of 0.76, the back pressure in the tunnel was adjusted such that the acceleration of the flow over the airfoil produced a supersonic region that terminated with a shockwave near the trailing edge of the airfoil. The shockwave formed on the airfoil extended to the roof of the tunnel generating a shockwave/boundary layer interaction region on the roof of the tunnel. In this region, a porous insert was placed beneath a closed plenum to examine the effect of passive porosity. The flat roof was chosen as the location of the passive control region to eliminate surface curvature effects in the interaction region.

The two-dimensional computational domain, partially shown in Figure 2, represents the true dimensions of the wind tunnel, 1200mm in length, 63mm in height, with a floor divergence of 0.4° beginning at the tunnel entrance (0mm). Flow travels from left to right, and a cell width space is

placed at block boundary locations for clarity. As both the floor and roof of the tunnel are modeled as solid walls, the grid is clustered on both the top and bottom of the computational domain to capture the details in the boundary layer. The porous region is located on the tunnel roof between $x/c=0.825$ and $x/c=1.075$ where the ratio of hole area to porous region area is 13.6%. In the computational solution, the location of the porous region is denoted in Figure 2 by the solid line just above the computational domain. The porous region is slightly shifted in the computational domain to allow for grid sequencing in obtaining the solution. In the calculation of the transpiration velocity in the porous region, Chokani and Squire used the Darcy law in the form

$$v_w = C(p_p - p_w)$$

with a permeability constant, $C=4.5 \times 10^{-3} m^2 s/kg$. The average density and pressure at the wall in the porous region were used to calculate an equivalent permeability factor for use in the equation presented in §2.4.1; $C_f=1.04$. Table 1 lists the additional geometric parameters outlined in the experiments that were used in the porosity models.

For a baseline, no passive control, solution, the pressure distribution on the roof of the tunnel is shown in Figure 3 compared to the experimental data. The Girimaji¹⁶ turbulence model is used for these tunnel simulations. The trend in the computational solution follows the experimental data. The Mach number and position of the shock are slightly under-predicted, but the shock is still positioned well within the region where passive control is to be applied. As the tunnel is long and narrow, the boundary layers on the walls of the tunnel are thick and play an important role in the shock interaction. Figure 4 shows the upper wall pressure distributions for flow with passive control for all porous wall models compared to the experimental data with passive control. The computational solutions again predict pressure distributions similar to that seen in the experiment.

The Darcy-constant and Darcy-sinusoidal models predict well the pressure relief seen in the porous region. The Darcy-geometric and Pipe flow models predict greater pressure relief in the porous region than the experiment. Downstream of the porous region, all porous model solutions converge to a wall pressure that is the same downstream pressure predicted in the baseline case. This return to a wall pressure that is the same as the baseline case is reflected in the experimental data as well.

The transpiration velocity distributions for all porous wall models are shown in Figure 5. The general trend for the transpiration velocity distributions is what one would expect. Negative wall velocities, representing flow from the freestream into the plenum, occur over the aft portion of the porous region, and positive wall velocities, representing flow from the plenum into the freestream, occur over the forward portion of the porous region. However, in Figure 5, all models but the Pipe flow model show a small region of negative wall velocities at the very beginning of the porous region. This unexpected region of flow into the plenum may be a result of inaccuracies in either the porous wall model, the calculation of plenum pressure, or an abrupt change in boundary condition from a solid wall to a permeable wall. The sensitivity of the permeability factor in the Darcy-constant and Darcy-sinusoidal models is shown in Figure 6 in the form of the transpiration velocity distributions. The permeability constant, C_f was changed from its original value of 1.04 to a value of 0.6. Both models show very little sensitivity to the large change in the permeability constant. At most, the change in transpiration velocity is on the order of $3m/s$. It can also be noted from the normal velocity curve that in all cases, the mass flow drawn into the cavity is equal to the mass flow blown out of the cavity, verifying the conservation of mass.

Mach number and density contour lines near the wall at the shock location are shown in Figure 7 for the baseline (no porosity) solution. The near-normal shock generated on the airfoil to impinges on the upper wall. Figures 8 and 9 show the same flowfield contours for solutions with

passive control using the Darcy-constant and Darcy-sinusoidal models, respectively. Density contours for both models show thickening of the boundary layer caused by the blowing of air into the freestream upstream of the shockwave, and movement of the shockwave toward the end of the porous region. A distinct oblique shockwave is not observed at the leading edge of the porous region, and the shockwave appears to penetrate the boundary layer closer to the wall than in the baseline solution. The results seen in Figure 10 for the Darcy-geometric porosity model are qualitatively in better agreement with experimental data of Chokani and Squire. The shockwave does not penetrate the boundary layer as close to the wall as in the baseline case, and the contour lines show the spreading out of the shock in the boundary layer. These are a result of transpiration velocities much greater in magnitude, as shown in Figure 5, for the Darcy-geometric model compared to the other models. Figure 11 shows the flowfield solutions for the non-linear Pipe flow model. Similar to the Darcy-geometric model, the penetration of the shockwave in the boundary layer is not as close to the wall as in the baseline case, however, the spreading of the shock seen in the Chokani and Squire experiment is less evident. The differences in the solutions obtained in this study compared to those obtained by Chokani and Squire may be a result of the use of different turbulence models (Chokani and Squire used the algebraic Baldwin-Lomax turbulence model) and different implementation of the porous boundary condition.

The results from the study of passive porosity on a flat plate indicate the Darcy-geometric and Pipe flow models better predict both the flow field characteristics and surface pressure distributions shown by the experiment.

3.1.2 Passive Control on a Circular Arc Airfoil

Bahi^{1,2} conducted an experimental study on the application of passive porosity on airfoils. Experimental tests were conducted on the flow over a 12%-thick, circular-arc airfoil with a

freestream Mach number of 0.83. The presence of the airfoil on the floor of the tunnel accelerates the flow producing a supersonic region over the airfoil. This supersonic region terminates in a shockwave located on the aft portion of the airfoil. A porous region was then placed on the airfoil from 57%-80% of the airfoil chord to examine the effects of passive porosity. The two-dimensional computational domain is shown in Figure 12. The entire computational domain extends approximately five chord lengths both upstream and downstream of the airfoil, as well as in the streamwise-normal direction.

For the baseline, non-porous case, the comparison of the Mach number distributions for the computational solution and experimental data is shown in Figure 13. The comparison is quite good. The shock is accurately captured at approximately 63% of the airfoil chord. As in the experiment, a porous region was then added from 57%-80% of the airfoil chord. A porous open area of 7% characterized the porosity. In characterizing the porosity in this study, a value of $C_f = 0.8$ was used for the constant and sinusoidal porosity models. Geometric parameters as outlined in Bahi's experiment, listed in Table 1, were used in the Darcy-geometric and Pipe flow models. The Mach number distributions for each porosity model are shown in Figure 14. Compared to the experimental data, a similar decrease is seen in the peak Mach number for all models except the Darcy-sinusoidal model. Flowfield Mach number and density contours near the location of the shock are shown in Figures 15 and 16 for the Darcy-geometric and Pipe flow models, respectively. The Mach number distributions for the porous solutions predict a weak oblique shock followed by a strong shock located near the aft of the porous region. Although not seen in the Bahi experiment, the computed Mach number distributions are similar to the distributions observed in the passive control experiments of Raghunathan and Mabey³.

To further evaluate the adequacy of the porous boundary condition, the velocity profile normal to the surface for each model is shown in Figure 17. The shape of the velocity distribution and velocity magnitudes are similar to those presented in experimental and computational work by Chokani and Squire⁵. The sensitivity of varying the porosity for the Darcy-constant model is shown in Figure 18; it is seen that an increase in the permeability factor corresponds to increased wall velocities in and out of the plenum. It can also be noted from the normal velocity curve that in all cases, the mass flow drawn into the cavity is equal to the mass flow blown out of the cavity, verifying the conservation of mass.

The results from the study of passive porosity on a circular arc airfoil support the indication that the Darcy-geometric and Pipe flow models perform better than the Darcy-constant and Darcy-sinusoidal models. The models predict the lambda shock structures and Mach number distributions seen in various passive porosity experiments.

3.2 Grid Dependence

A grid sequencing technique is used to obtain the solutions in this study. When the grid is generated, its dimensions are chosen as multiples of four. The coarse, medium, and fine grids are then obtained in the following manner. For a coarse grid solution, denoted *444* for a three-dimensional grid and *144* for a two-dimensional grid, every fourth grid point is used in obtaining the solution. For a medium grid solution (*222* or *122*), the solution is obtained using every other grid point. Finally, on a fine grid, *111*, the solution are obtained with every grid point. The solutions at each grid level are converged before sequencing to the next grid level. Using this grid sequencing technique saves time in obtaining solutions as it allows major flow characteristics to develop on a coarse grid, followed by the development of smaller scale characteristics in the medium and fine grid solutions.

The two-dimensional afterbody computational domain has overall coarse, medium, and fine grid levels of dimensions 186×71 , 372×142 , and 744×284 . A grid refinement study was conducted on this two-dimensional computational domain which consisted of 11 blocks. The grid dimensions of each block are shown in Table 2. Figure 19 shows the effect of grid refinement on the performance parameters for the 20° nozzle with $M_x=0.6$ and $NPR=6$ with porosity using the Darcy-constant porosity model. This case is representative of the results for all solutions examined. There is very little change in the discharge coefficient and axial thrust ratio from the medium grid to the fine grid, indicating that the results are grid independent.

3.3 Solution Convergence

For the nozzle studies presented herein, both the residual and nozzle performance characteristics were used to assess the solution convergence. Nozzle performance quantities such as the discharge coefficient and the internal thrust ratio were analyzed using the nozzle performance package developed by Carlson²⁰. As a representative case, the results for the $M_x=0.6$, $NPR=6$, 20° nozzle flow with porosity and the Darcy-constant model are used. Figure 20 shows the convergence histories for the discharge coefficient and the axial thrust ratio. The discharge coefficient and thrust ratio are shown to converge on each grid level (coarse, medium, and fine). Over each grid level, there is an approximate order of magnitude drop in the residual as shown in Figure 21.

3.4 Two-Dimensional Subsonic Computations

The two-dimensional simulations obtained for the afterbody geometry were for a subsonic freestream Mach number, $M_x=0.6$, and a nozzle pressure ratio, $NPR=6$. The two-dimensional computational domain for the 10° nozzle afterbody is shown in Figure 22, noting that only every 5th grid line is shown to enable easy viewing. The entire domain extends approximately 20 model lengths both upstream and downstream of the model, as well as in a stream-wise normal direction.

A comparison of the pressure distribution for the experimental data and computational solution for the 10°, 20°, and 30° nozzles without control is presented in Figure 23. In all cases, the computation under-predicts the pressure recovery on the forward portion of the nozzle. As the nozzle cross-sections in the experiment are rectangular in shape, the discrepancy between the two-dimensional computational solutions and the experimental data may be due to three-dimensional effects present in the experiment. These effects may be more pronounced near the shoulder of the nozzle. The porous region on the afterbody was initially placed from 20%-60% of the nozzle length. This location coincided with the largest pressure gradient observed in the experimental data. A permeability factor of $C_f=0.8$ was used in the constant and sinusoidal porosity models. Table 1 shows the geometric parameters used for the Darcy-geometric and Pipe flow models in all afterbody computations; these are based on the conditions for the proposed experiment at NASA Langley Research Center.

The effect of porosity on the pressure distributions for the 10°, 20°, and 30° nozzles, both solid and porous, are compared in Figure 24. For the 10° nozzle, the addition of porosity using the Darcy-constant and Darcy-sinusoidal porosity models predict a loss of pressure recovery, while the expansion over the forward portion of the nozzle is the same as the baseline case. The Darcy-geometric porosity model, however, predicts an increase in the pressure recovery with a decrease in the expansion over the nozzle shoulder. For the 20° nozzle, the addition of porosity using all models predicts a decrease in the nozzle expansion but a loss in pressure recovery compared to the baseline case. In the 30° nozzle case, all models predict little change in pressure recovery, and the pressure distributions are quite similar. An exception, however, is the Darcy-geometric model that predicts an over-expansion of the nozzle shoulder. Although the effects of porosity may appear adverse in terms of pressure recovery, the loss does not appear significant. It should be kept in

mind that the primary objective of using passive porosity is to alleviate the adverse effects of shockwave/boundary layer interactions. Thus, a subsonic case is considered an off-design case for the application of passive porosity.

Figure 25 shows the effect of the porosity model on the distribution of the transpiration velocity for the 10° , 20° , and 30° nozzles. Flow suction occurs over the aft portion of the porous surface, identified by negative wall velocities, and flow is injected back into the external flow over the forward portion. The transpiration velocity distributions are in general linear. These linear distributions differ from the velocity distributions over the circular arc airfoil in Figure 17. The distributions over the circular arc airfoil are the result of a shockwave, i.e. an abrupt pressure change. Since there is no shockwave present in a subsonic nozzle flowfield, the pressure changes over the nozzles are gradual, resulting in the linear transpiration velocity distribution.

Table 3 contains the afterbody pressure drag coefficients for all nozzles with and without porosity. For the 10° nozzle, the baseline case has the lowest coefficient of drag when compared to the porous afterbody using all four models. The loss in pressure recovery shown by the models for the 10° nozzle results in higher drag. For the 20° and 30° nozzles, some models predict drag reduction while others predict increases in drag. Reduction in drag as a result of passive porosity at a subsonic, off-design, case, would be an added advantage due to the reductions that potentially exist at a design (that is, transonic) Mach number.

3.5 Effect of Porous Placement

The effect of the placement of the porous surface was next investigated for the 20° and 30° nozzles. The higher angle nozzles were chosen to exploit the increased expansion across the nozzle shoulder. The porous region was moved forward to 0%-40% of the nozzle length; note that the

extent of the porosity was kept fixed. The Darcy-geometric and Pipe flow models were used to examine the effect of porous placement.

The resulting pressure distribution for the 20° nozzle is shown in Figure 26. Both models show a smaller expansion and loss in pressure recovery. The two models also show quite similar behavior. In the case of the 30° nozzle, Figure 27, the expansion is delayed downstream of the nozzle shoulder, and is predicted aft for the Darcy-geometric model. The overall pressure recovery is similar in both cases. The corresponding transpiration velocity distributions for the 20° and 30° nozzles are shown in Figures 28 and 29, respectively. For the 20° nozzle, the Darcy-geometric model predicts velocities twice the magnitude of the predicted Pipe flow velocities. In contrast, for the 30° nozzle, it is the Pipe flow velocities that are twice the magnitude of the Darcy-geometric velocities. In both cases, the overall magnitude of the velocities are greater than those seen in the original porous placement case.

From the results for placing the porous region from 0%-40% of the nozzle length, gains in pressure recovery appear to be more significant for the 30° nozzle, but a greater relief of the initial expansion is observed for the 20° nozzle. The initial expansion of the flow over the nozzle may prove problematic in the plenum as, for the 30° nozzle, low velocity flow is seen to enter the plenum at the beginning of the porous region. Placing the porous region from 0%-40% of the nozzle length also results in higher predicted drag as shown in Table 4. The result of additional drag would have to be weighed against advantages present at design conditions.

3.6 Effect of Porous Extent

It is desirable to keep the porous region as small as possible, without reducing its effectiveness; thus, the porous region was reduced in size extending from 20%-40% of the nozzle length. This location of the porosity was again chosen in an attempt to exploit the expansion of the flow over the

nozzle. The effect of the porosity on the 20° nozzle for the two models, Figure 30, is almost the same, showing the same expansion and loss in recovery over the nozzle. For the 30° nozzle, Figure 31, both models predict a slight gain in pressure recovery compared to the baseline case. In addition to the gain in predicted pressure recovery, the Darcy-geometric model predicts a smaller expansion over the nozzle shoulder.

The transpiration velocity distributions for the 20° and 30° nozzles are shown in Figures 32 and 33, respectively. The predicted velocities on the 20° nozzle are greater for the Darcy-geometric model, but similar in both cases to the predicted velocities of the 20%-60% porous region. Similarly, the distributions on the 30° nozzle are similar both in shape and magnitude to each other, and to the results seen for the porous region from 20%-60% of the nozzle length.

The afterbody pressure drag coefficients for the above mentioned cases are shown in Table 5, and in all but one case, predict a reduction in drag with the addition of passive control. Reducing the size of the porous region is seen to not reduce the effectiveness of the passive porosity. The reduced region shows increased pressure relief over the nozzle as well as increases in pressure recovery on the 30° nozzle, and decreases in drag at an off-design condition would be an addition to advantages present at design conditions.

3.7 Three-Dimensional Computations

As previously shown in Figure 23, the two-dimensional solutions under-predicted the pressure recovery on the afterbody. The two-dimensional computations were considered due to the high aspect ratio (ratio of width to height) of the nozzle exit, 6.39 (exit height of 1.35cm and width of 8.64cm), for the 20° boat-tail angle. On the other hand, the afterbody has a low aspect ratio at the nozzle-connect, 1.097 (connect height of 7.87cm and width of 8.64cm). The under-prediction in the two-dimensional solution may be a result of pressure relief around the side of the afterbody. To

investigate the three-dimensional effects associated with the afterbody, the three-dimensional grid shown in Figure 34 was generated. The grid represents the actual experimental configuration with the twenty-degree afterbody and symmetry planes as noted.

Using the three-dimensional computational domain, the same subsonic flow conditions, $M_x=0.6$ and $NPR=6$, were used to obtain a three dimensional solution. The surface pressure distribution along the centerline of the afterbody is shown in Figure 35 compared to both the two-dimensional solution and experimental data. The three-dimensional solution is in better agreement with the experimental data. The marked difference in surface pressure distribution between the two- and three-dimensional solutions illustrates the three-dimensional effects associated with the afterbody flow. The drag calculated from the computational solution also confirms the importance of the three-dimensional effects in afterbody flow. The experimental nozzle pressure drag coefficient is 0.0596, and the three-dimensional solution predicted a nozzle pressure drag coefficient of 0.0606. The slight difference of 0.001 further emphasizes the accuracy of the three-dimensional distribution. The under-prediction of the pressure recovery by the two-dimensional solution results in a predicted nozzle pressure drag coefficient of 0.1686, almost three times the measured experimental nozzle pressure drag.

Figure 36 illustrates the centerline surface pressure distributions at a supersonic freestream Mach number of $M_x=1.2$. The three-dimensional solution follows the experimental data very well. The measured experimental nozzle pressure drag coefficient is 0.2465, and the predicted nozzle pressure drag coefficient is 0.2144. The smaller predicted drag coefficient by the three-dimensional solution is consistent with the pressure distribution in Figure 36, as the pressure drag coefficient is representative of the area under the pressure distribution. The three-dimensional effects associated

with the rectangular boat-tail afterbody are significant. Hence, the two-dimensional assumption for the afterbody flow may introduce error, and not accurately represent true flowfield solution.

4. Concluding Remarks

A computational investigation of afterbody flow using a passive control method has been conducted. The code, *PAB3D*, was used to simulate the effects of passive porosity on an aircraft afterbody. Four different boundary conditions were used to model the transpiration velocity in the region of passive control. The four boundary conditions were first tested on a flat surface and an airfoil examined in two previous experimental studies on passive porosity. Pressure relief predicted by the models in the regions of passive control represented well the trends and magnitudes shown by the experimental data. Transpiration velocity distributions illustrate the natural suction and blowing associated with the passive porosity concept and are consistent in magnitude with experimental findings.

Afterbody configurations with 10°, 20°, and 30° boat-tail angles were used to obtain computational solutions. Surface pressure distributions for baseline (no porosity) cases at a freestream Mach number of 0.6 were compared to experimental data. Two-dimensional simulations predicted the same pressure recovery trend as shown by the experimental data, but in magnitude, under-predicted the recovery on the nozzle. The under-prediction of the pressure recovery on the nozzle resulted in nozzle pressure drag predictions almost three times that shown by the experiment. Passive control was then added on the nozzle in the region of 20%-60% of the nozzle length. Solutions with passive control for the subsonic freestream Mach number showed porosity models predict changes in the surface pressure distribution including reduced expansion of the flow over the nozzle and losses in pressure recovery. Placement and extent of the porous region has also been shown to influence the effect of porosity. As passive porosity applied in a purely subsonic flow is considered an off-design case, losses seen in the two-dimensional subsonic solutions would have to be weighed against advantages that might be present at transonic (design) conditions.

As the two-dimensional solutions under-predict the pressure recovery on the afterbody compared to the experimental data, three-dimensional effects were investigated as the cause of the under-prediction. The afterbody configuration is rectangular, and pressure relief around the side of the afterbody plays a significant role in the flow. A three-dimensional grid was generated to obtain solutions for comparison with the two-dimensional solutions. Three-dimensional, baseline solutions showed significant improvement in representing the pressure relief shown by the experimental data. Very little error is seen in the drag predictions from the three-dimensional solutions. Hence, the afterbody flow is shown to be three-dimensional in nature.

As three-dimensional effects have been shown an important part of the afterbody flow, in future work, passive porosity should be examined in a three-dimensional computation. Accurate representation of the flow physics is essential in determining true advantages of the passive porosity control method. Drag predictions must be accurate for baseline cases before reductions in drag as a result of passive control can be ascertained. The effects of passive porosity should also be examined on the afterbody in the presence of a shockwave resulting from transonic and supersonic freestream Mach numbers. Different porous region configurations and placements should be considered, and results compared to passive porosity experimental tests planned in the future.

5. References

1. Bahi, L., Ross, J.M., and Nagamatsu, H.T., "Passive Shock Wave/Boundary Layer Control for Transonic Airfoil Drag Reduction," *AIAA Paper 83-0137*, Jan. 1983.
2. Bahi, L., "Passive Shock Wave/Boundary Layer Control for Transonic Supercritical Airfoil Drag Reduction," Ph.D. Thesis, Rensselaer Polytechnic Institute, May 1982.
3. Raghunathan, S., and Mabey, D.G., "Passive Shock-Wave/Boundary-Layer Control on a Wall-Mounted Model," *AIAA Journal*, Vol. 25, Feb. 1987, pp. 275-278.
4. Bauer, S.X.S., and Hemsch, M.J., "Alleviation of Side Force on Tangent-Ogive Forebodies Using Passive Porosity," *Journal of Aircraft*, Vol. 31, Mar.-Apr. 1994, pp. 354-361.
5. Chokani, N., and Squire, L.C., "Transonic Shockwave/Turbulent Boundary Layer Interactions on a Porous Surface," *Aeronautical Journal*, May 1993, pp. 163-170.
6. Hanna, R.L., "Hypersonic Shockwave/Turbulent Boundary Layer Interactions on a Porous Surface," *AIAA Paper 95-0005*, Jan. 1995.
7. Idel'cik, "Memento Des Pertes de Charge," Eyrolles, Paris, 1969.
8. Abdol-Hamid, K. S., "A Multiblock/Multizone Code (PAB3D-v2) for the Three-Dimensional Navier-Stokes Equations: Preliminary Applications," *NASA CR-182032*, Oct. 1990.
9. Abdol-Hamid, K. S., Carlson, J. R., and Pao, S. P., "Calculation of Turbulent Flows Using Mesh Sequencing and Conservative Patch Algorithm," *AIAA Paper 95-2336*, July 1995.
10. Abdol-Hamid, K. S., "Application of a Multiblock/Multizone Code(PAB3D) for the Three-Dimensional Navier-Stokes Equations," *AIAA Paper 91-2155*, July 1991.
11. Abdol-Hamid, K. S., Carlson, J. R., and Lakshmanan, B., "Application of Navier-Stokes Code PAB3D With $k-\varepsilon$ Turbulence Model to Attached and Separated Flows," *NASA TP-3480*, Jan. 1995.

- ¹². Abdol-Hamid, K. S., "Implementation of Algebraic Stress Model in a General 3-D Navier-Stokes Method (PAB3D)," *NASA CR-4702*, Dec. 1995.
- ¹³. Carlson, J. R., "High Reynolds Number Analysis of Flat Plate and Separated Afterbody Flow Using Non-Linear Turbulence Models," *AIAA Paper 96-2544*, July 1996.
- ¹⁴. Jones, W. P. and Launder, B.E., "The Prediction of Laminarization With a Two-Equation Model of Turbulence," *Int. J. Heat & Mass Trans*, Vol. 15, Feb. 1972, pp. 301-314.
- ¹⁵. Shih, T-H., Zhu, J., and Lumley, J.L., "A New Reynolds Stress Algebraic Model," *NASA TM-166644*, ICOMP 94-8, 1994.
- ¹⁶. Girimaji, S. S., "Fully-explicit and Self-consistent algebraic Reynolds Stress Model," *ICASE Report 95-82*, 1995.
- ¹⁷. Poll, D.I.A., and Danks, M., "The Aerodynamic Performance of Laser Drilled Sheets," *STAR*, Vol. 31, July 1993, pp. 274-277.
- ¹⁸. Carlson, J. R., and Asbury, S.C., "Two-Dimensional Converging-Diverging Rippled Nozzles at Transonic Speeds," *NASA TP-3440*, July 1994.
- ¹⁹. Staff of the Propulsion Aerodynamics Branch, "A Users' Guide to the Langley 16-Foot Transonic Tunnel Complex, Revision 1," *NASA TM-102750*, 1990.
- ²⁰. Pao, S. P., "Users' Guide to the Axb Grid Generator," 1994 (unpublished).
- ²¹. Carlson, J. R., "A Nozzle Internal Performance Prediction Method," *NASA TP-3221*, 1992.

6. Tables

Parameter	Chokani & Squire ⁵	Bahi ^{1,2}	Afterbody (present work)
d	0.032in	0.0121in	0.02in
t_h	0.0118in	0.125in	0.125in
H	1	1	1
P	0.136	0.06	0.20

Table 1:
Geometric parameters used in Porous Wall Models

Block No.	1	2	3	4	5	6
<i>111(Fine)</i>	169×157	21×65	97×65	149×157	97×157	97×65
<i>122(Medium)</i>	85×79	11×33	49×33	75×79	49×79	49×33
<i>144(Coarse)</i>	43×39	5×17	25×17	37×39	25×39	25×17

Block No.	7	8	9	10	11
<i>111(Fine)</i>	97×65	41×65	109×157	97×157	129×157
<i>122(Medium)</i>	49×33	21×33	55×79	49×79	65×79
<i>144(Coarse)</i>	25×17	11×17	27×39	25×39	33×39

Table 2:
Two-Dimensional Afterbody Grid Dimensions

Porous model	10° Nozzle	20° Nozzle	30° Nozzle
<i>Baseline</i>	.065	.169	.293
<i>Darcy-constant</i>	.070	.175	.269
<i>Darcy-sinusoidal</i>	.069	.167	.291
<i>Darcy-geometric</i>	.069	.259	.289
<i>Pipe flow</i>	.068	.152	.281

Table 3:
Afterbody Pressure Drag Coefficients for Passive Porosity from 20-60% of Afterbody Length

Porous model	20° Nozzle	30° Nozzle
<i>Baseline</i>	.169	.293
<i>Darcy-geometric</i>	.194	.354
<i>Pipe flow</i>	.187	.321

Table 4:
Afterbody Pressure Drag Coefficients for Passive Porosity from 0-40% of Afterbody Length

Porous model	20° Nozzle	30° Nozzle
<i>Baseline</i>	.169	.293
<i>Darcy-geometric</i>	.154	.298
<i>Pipe flow</i>	.156	.285

Table 5:
Afterbody Pressure Drag Coefficients for Passive Porosity from 20-40% of Afterbody Length

Appendix A

Navier-Stokes Equations

The governing equations in *PAB3D* are the three-dimensional, time-dependent, Reynolds-averaged simplified Navier-Stokes equations obtained by neglecting all streamwise derivatives of the viscous terms. In generalized coordinates and conservation form, the simplified Navier-Stokes equation is

$$\hat{Q}_t + \hat{F}_\xi + \hat{G}_\eta + \hat{H}_\zeta = 0$$

where

$$\begin{aligned}\hat{Q} &= \frac{Q}{J} \\ \hat{F} &= \frac{1}{J} (\xi_t Q + \xi_x F + \xi_y G + \xi_z H) \\ \hat{G} &= \frac{1}{J} (\eta_t Q + \eta_x F + \eta_y G + \eta_z H) \\ \hat{H} &= \frac{1}{J} (\zeta_t Q + \zeta_x F + \zeta_y G + \zeta_z H)\end{aligned}$$

with generalized coordinates

$$\begin{aligned}\xi &= \xi(x, y, z, t) = \text{Streamwise (marching) direction} \\ \eta &= \eta(x, y, z, t) = \text{Spanwise or circumferential direction} \\ \zeta &= \zeta(x, y, z, t) = \text{Normal direction}\end{aligned}$$

and their derivatives

$$\begin{aligned}\xi_t &= -(\xi_x x_t + \xi_y y_t + \xi_z z_t) \\ \eta_t &= -(\eta_x x_t + \eta_y y_t + \eta_z z_t) \\ \zeta_t &= -(\zeta_x x_t + \zeta_y y_t + \zeta_z z_t)\end{aligned}$$

The vector quantities in the governing equations are defined by

$$Q = \begin{pmatrix} \rho \\ \rho u \\ \rho v \\ \rho w \\ e \end{pmatrix} \quad F = \begin{pmatrix} \rho u \\ \rho u^2 + p \\ \rho uv \\ \rho uw \\ (e + p)u \end{pmatrix} \quad G = \begin{pmatrix} \rho v \\ \rho uv \\ \rho v^2 + p \\ \rho vw \\ (e + p)v \end{pmatrix} \quad H = \begin{pmatrix} \rho w \\ \rho uw \\ \rho vw \\ \rho w^2 + p \\ (e + p)w \end{pmatrix}$$

and the pressure is related to the energy by

$$p = (\gamma - 1) \left[e - \frac{1}{2} \rho (u^2 + v^2 + w^2) \right]$$

The viscous terms are defined as

$$F_v = \begin{pmatrix} 0 \\ \tau_{xx} \\ \tau_{xy} \\ \tau_{xz} \\ \frac{\gamma}{\text{Pr}} k \frac{\partial T}{\partial x} + u \tau_{xx} + v \tau_{xy} + w \tau_{xz} \end{pmatrix}$$

$$G_v = \begin{pmatrix} 0 \\ \tau_{yx} \\ \tau_{yy} \\ \tau_{yz} \\ \frac{\gamma}{\text{Pr}} k \frac{\partial T}{\partial y} + u \tau_{yx} + v \tau_{yy} + w \tau_{yz} \end{pmatrix}$$

$$H_v = \begin{pmatrix} 0 \\ \tau_{zx} \\ \tau_{zy} \\ \tau_{zz} \\ \frac{\gamma}{\text{Pr}} k \frac{\partial T}{\partial z} + u \tau_{zx} + v \tau_{zy} + w \tau_{zz} \end{pmatrix}$$

where shear stress terms are defined as the sum of the laminar and turbulent shear stresses; for example,

$$\tau_{xy} = \tau_{xy}^L + \tau_{xy}^T$$

The laminar shear stress terms are given by

$$\tau_{xy}^L = \frac{2}{3} \mu \left(2 \frac{\partial u}{\partial x} - \frac{\partial v}{\partial y} - \frac{\partial w}{\partial z} \right)$$

$$\tau_{xy}^L = \mu \left(\frac{\partial u}{\partial y} + \frac{\partial v}{\partial x} \right)$$

$$\tau_{yx}^L = \frac{2}{3} \mu \left(2 \frac{\partial v}{\partial y} - \frac{\partial u}{\partial x} - \frac{\partial w}{\partial z} \right)$$

$$\tau_{xz}^L = \mu \left(\frac{\partial u}{\partial z} + \frac{\partial w}{\partial x} \right)$$

$$\tau_{zz}^L = \frac{2}{3} \mu \left(2 \frac{\partial w}{\partial z} - \frac{\partial u}{\partial x} - \frac{\partial v}{\partial y} \right)$$

$$\tau_{yz}^L = \mu \left(\frac{\partial v}{\partial z} + \frac{\partial w}{\partial y} \right)$$

and the turbulent shear stress terms are determined from the turbulence model.
The Jacobian of the transformation, J is given by

$$J = \det \left(\frac{\partial(\xi, \eta, \zeta)}{\partial(x, y, z)} \right)$$

and the Prandtl number, Pr is given by

$$Pr = \frac{\mu C_{cp}}{k}$$

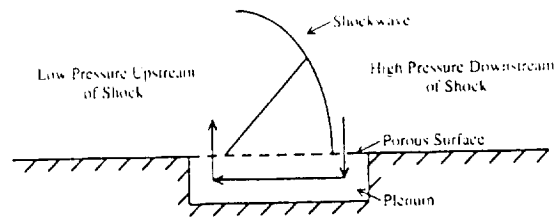


Figure 1: Passive Porosity Concept

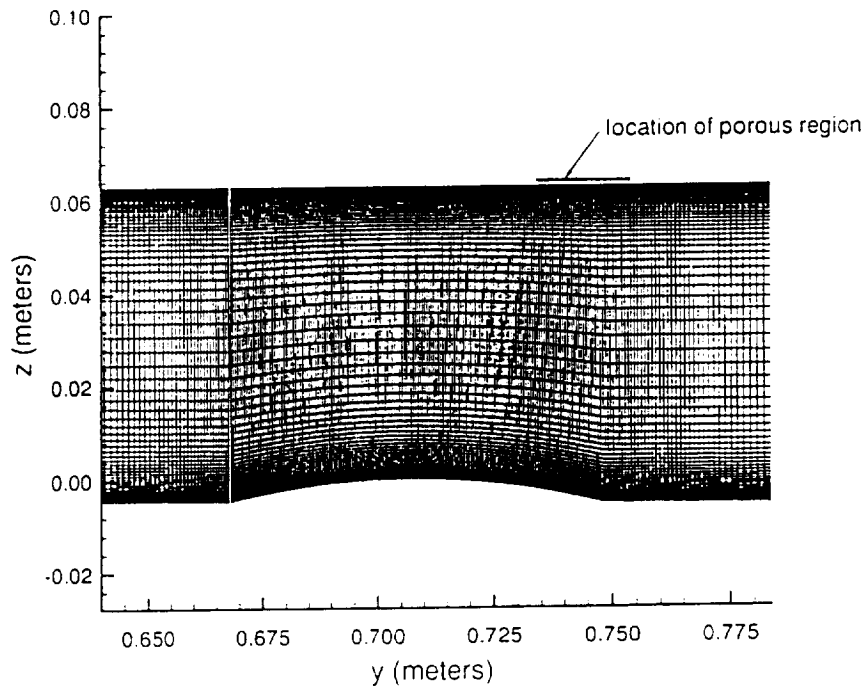


Figure 2: Two-Dimensional Grid; Chokani and Squire Experimental Set-up

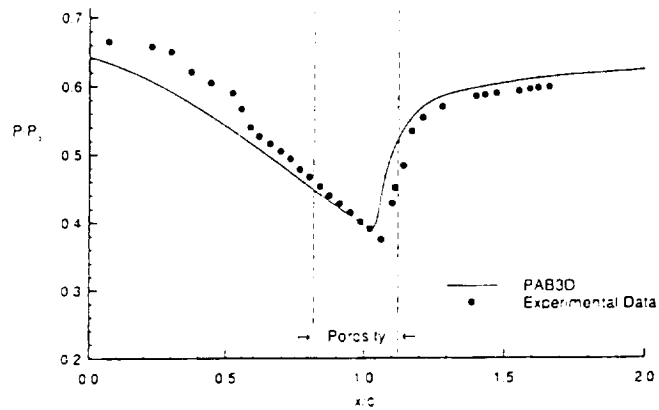


Figure 3: Comparison of Baseline Computational and Experimental Results for Chokani and Squire Experiment

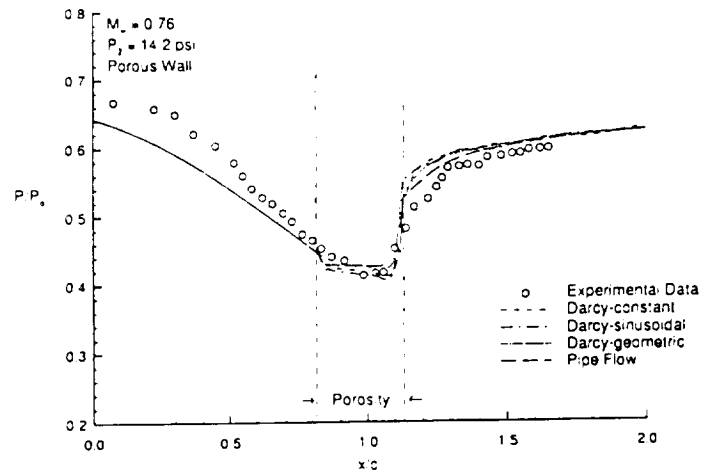


Figure 4: Comparison of Porous Computational and Experimental Results for Chokani and Squire Experiment

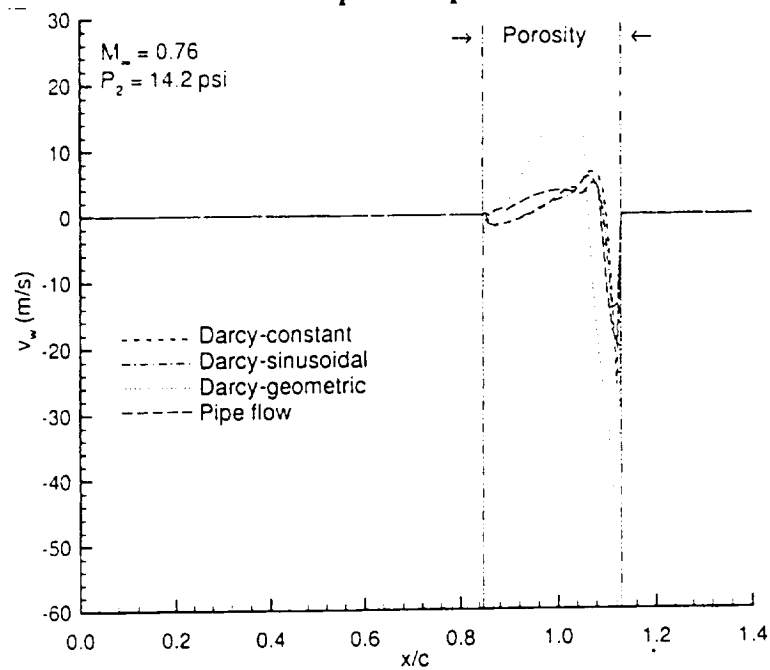


Figure 5: Transpiration Velocity Distributions for Porous Wall Models from Chokani and Squire Solutions

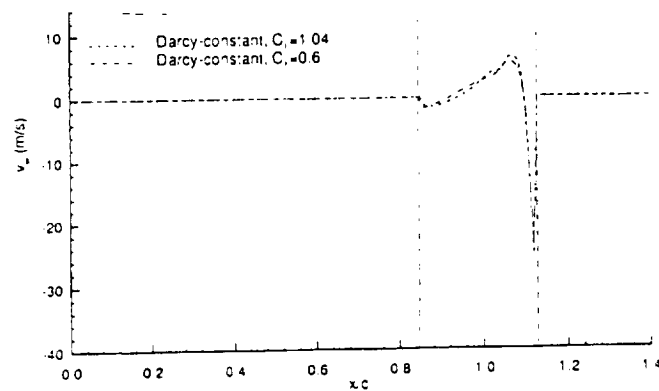


Figure 6a: Transpiration Velocity Showing Sensitivity of Permeability Factor C_1 for the Darcy-constant Porous Wall Model

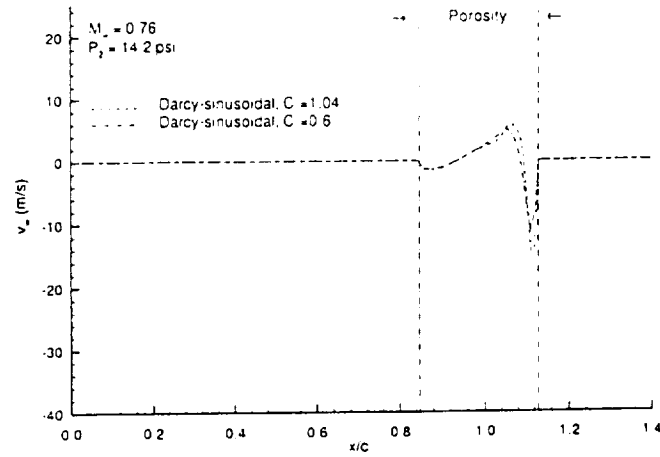


Figure 6b: Transpiration Velocity Showing Sensitivity of Permeability Factor C_1 for the Darcy-sinusoidal Porous Wall Model

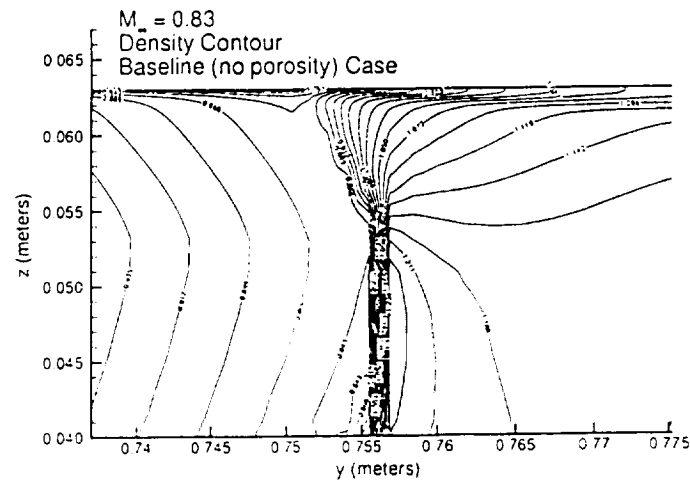
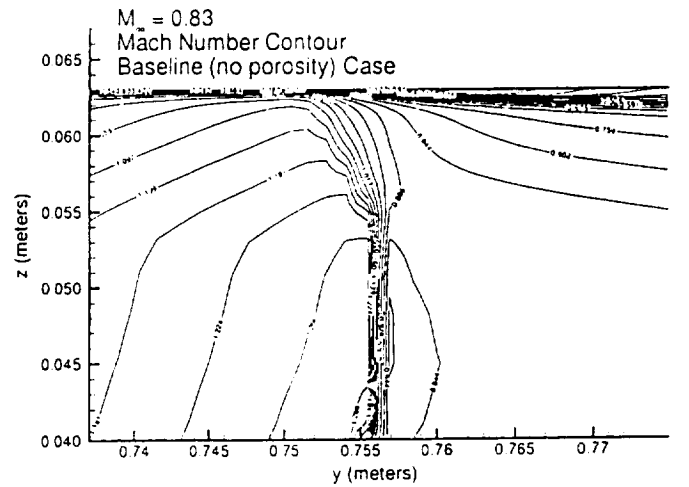


Figure 7: a) Mach Number and b) Density Contours for the Baseline (no porosity) Solution

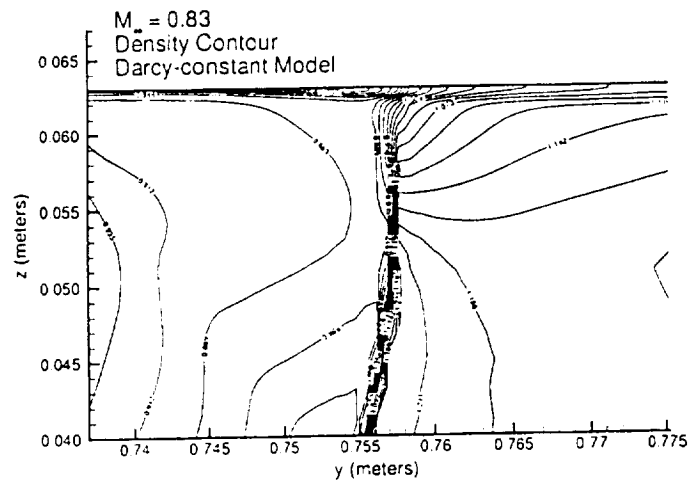
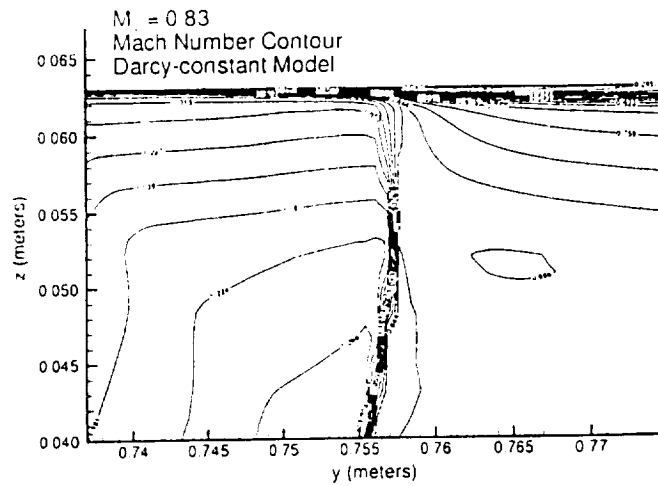


Figure 8: a) Mach Number and b) Density Contours for the Darcy-constant Porous Wall Model Solution

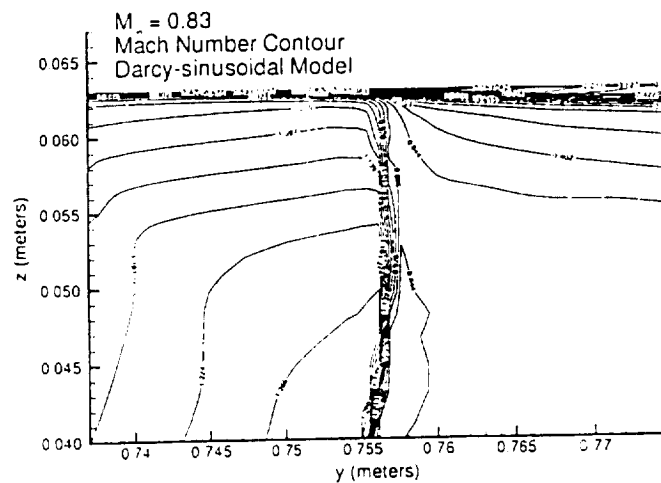


Figure 9a) Mach Number Contours for the Darcy-sinusoidal Porous Wall Model Solution

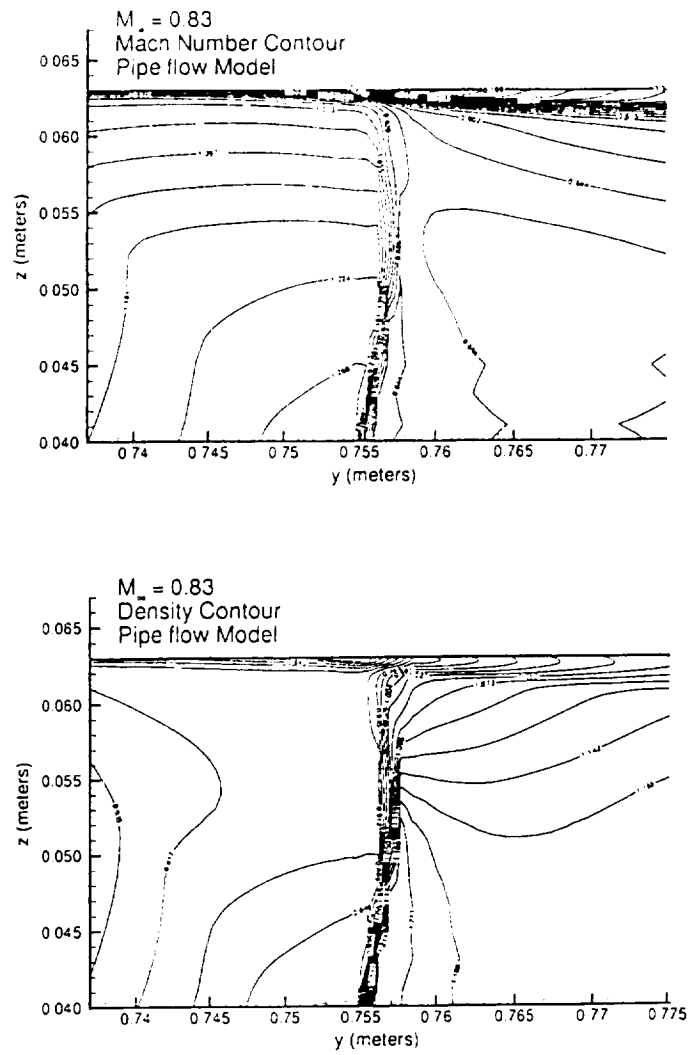


Figure 11: a) Mach Number and b) Density Contours for the Pipe flow Porous Wall Model Solution

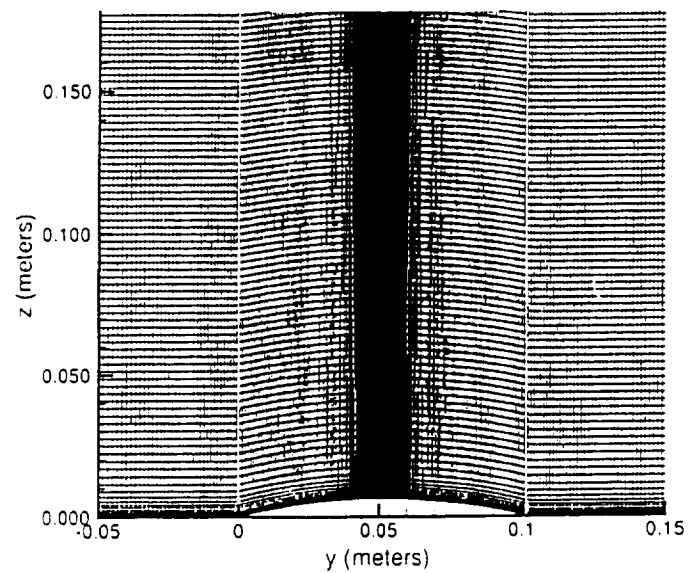


Figure 12: Two-Dimensional Grid; Bahi Experimental Set-up

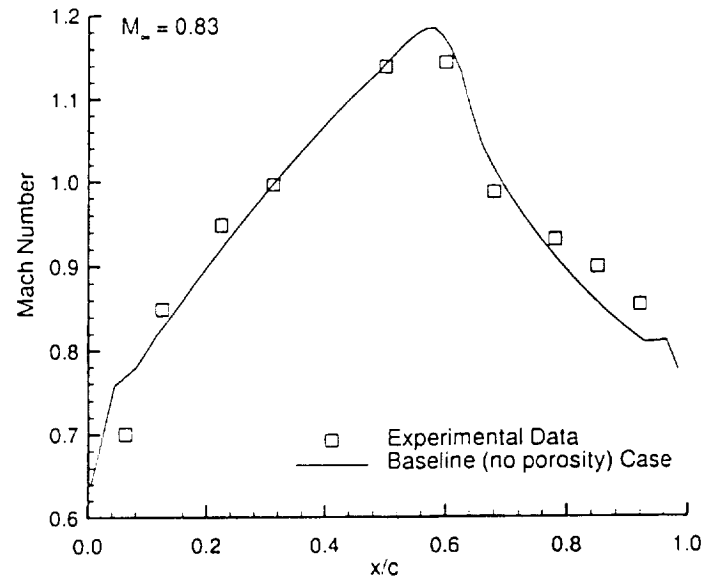


Figure 13: Comparison of Baseline Computational and Experimental Results for Bahi Experiment

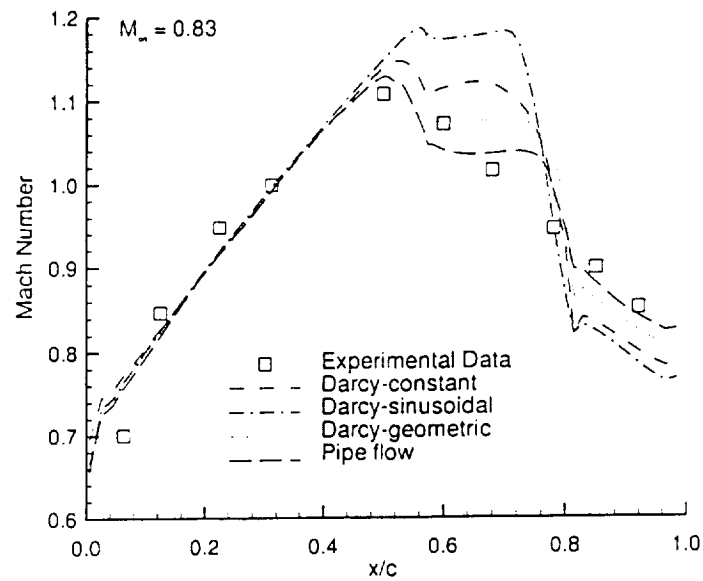


Figure 14: Comparison of Porous Computational and Experimental Results for Bahi Experiment

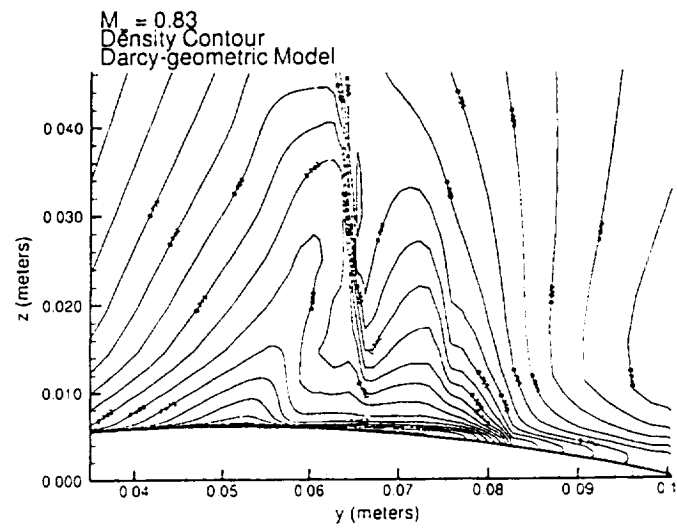
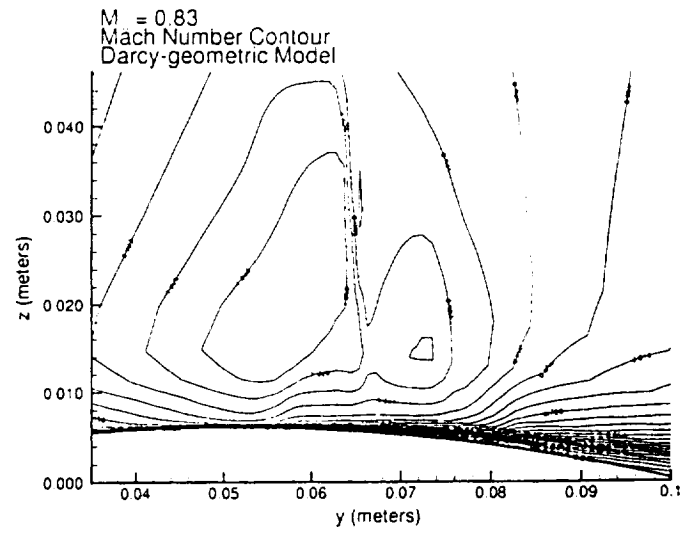


Figure 15: a) Mach Number and b) Density Contours for the Darcy-geometric Porous Wall Model Solution

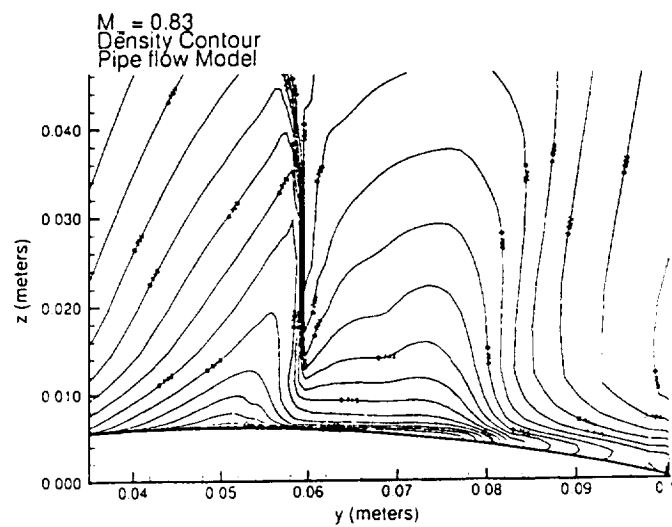
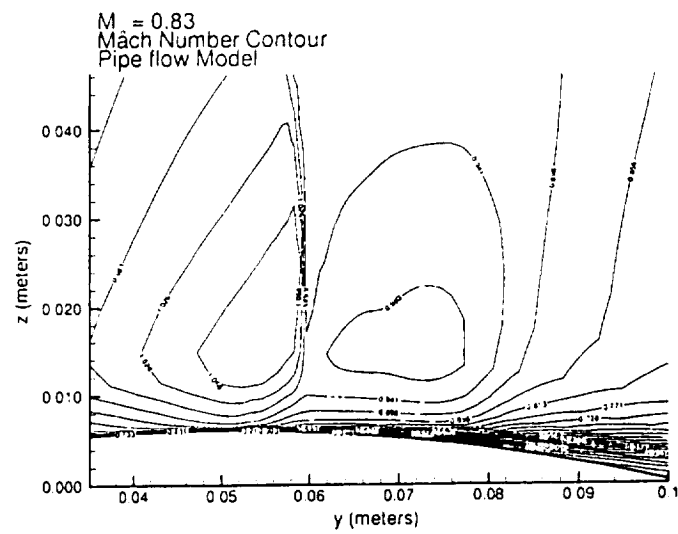


Figure 16: a) Mach Number and b) Density Contours for the Pipe flow Porous Wall Model Solution

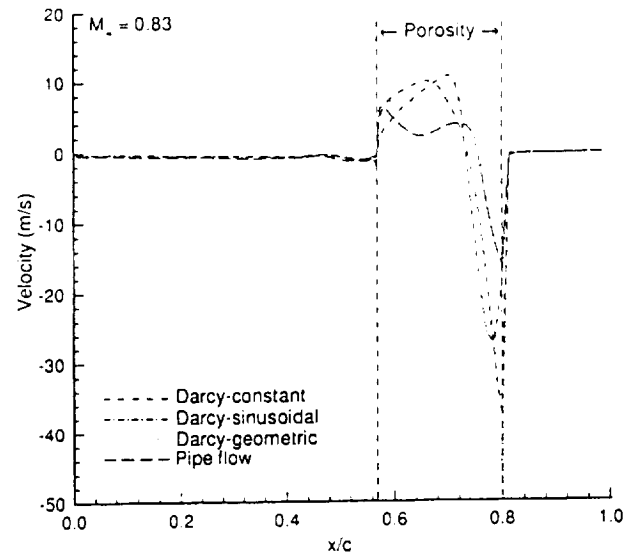


Figure 17: Comparison of Transpiration Velocity Results for Bahi Experiment

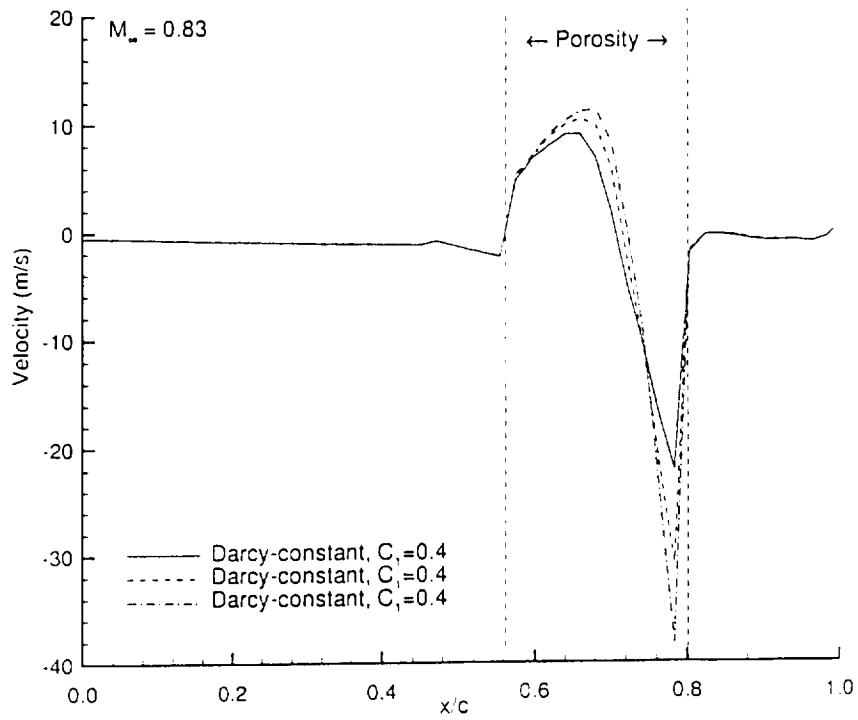


Figure 18: Comparison of Transpiration Velocity Results for Bahi Experiment

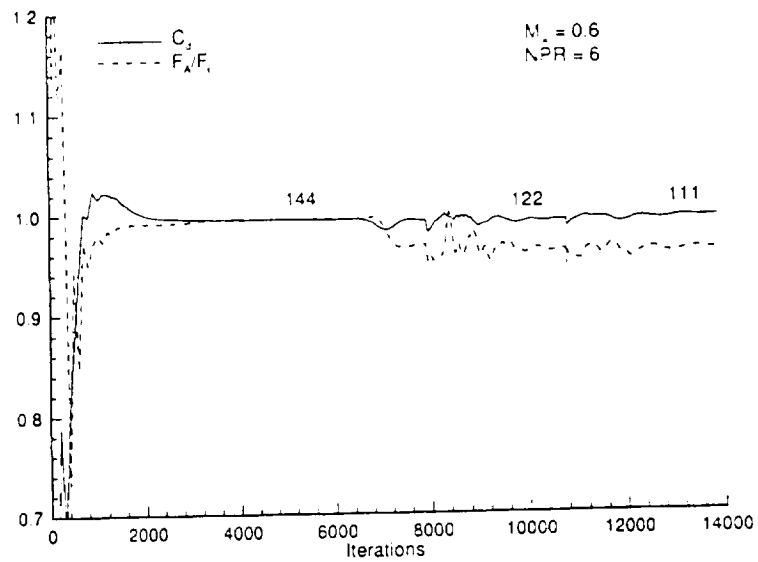


Figure 19: Effect of Grid Refinement on 20 deg Nozzle Solution

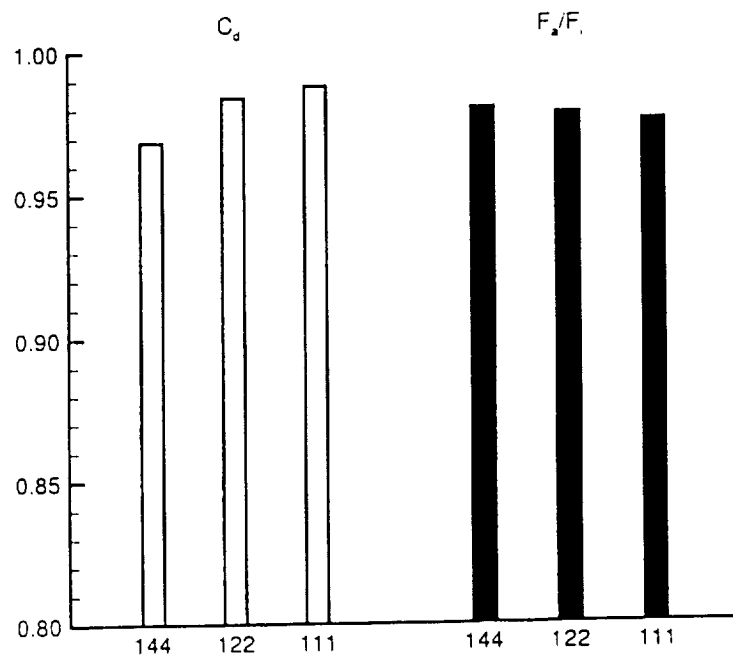


Figure 20: Performance Parameter Convergence of Representative Afterbody Solution

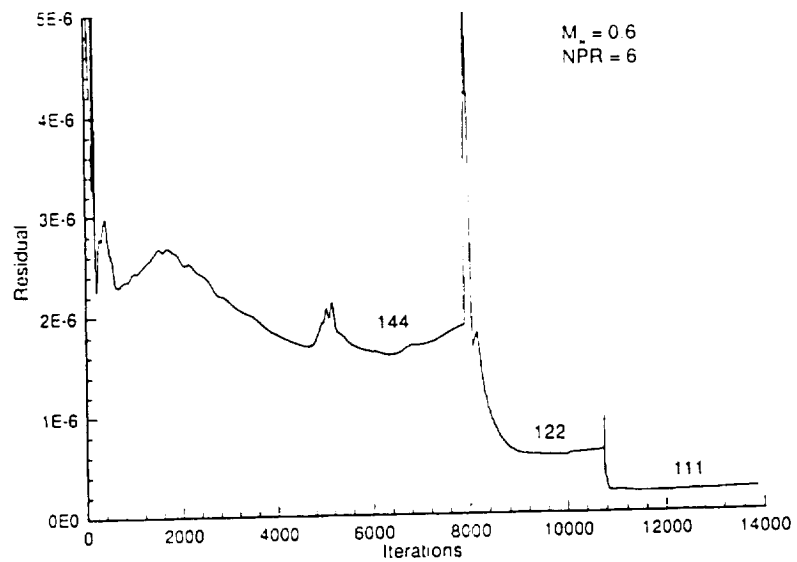


Figure 21: Residual History of Representative Afterbody Solution

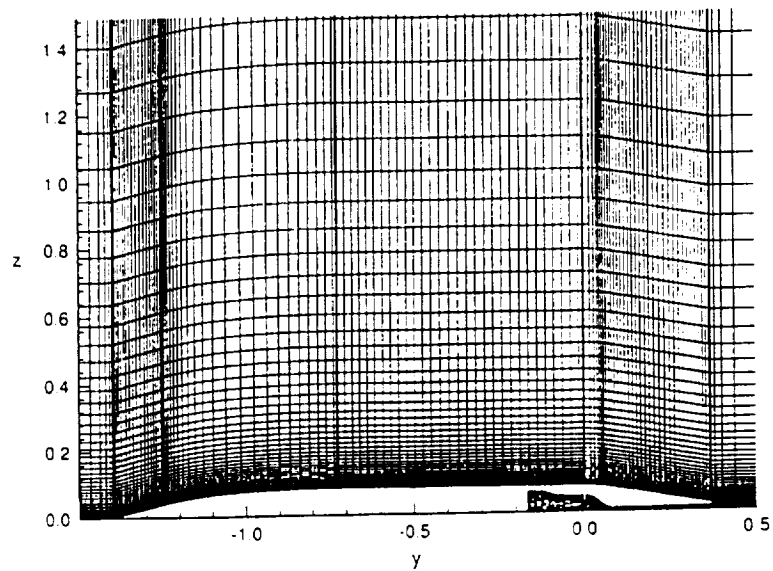


Figure 22: Two-Dimensional Multiblock Grid of Afterbody Configuration (for clarity, only every 5th gridline is shown in streamwise-normal direction)

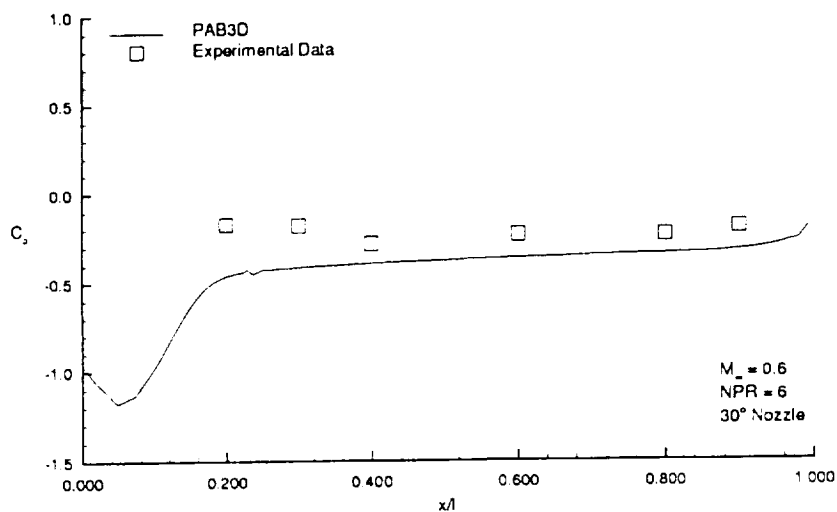
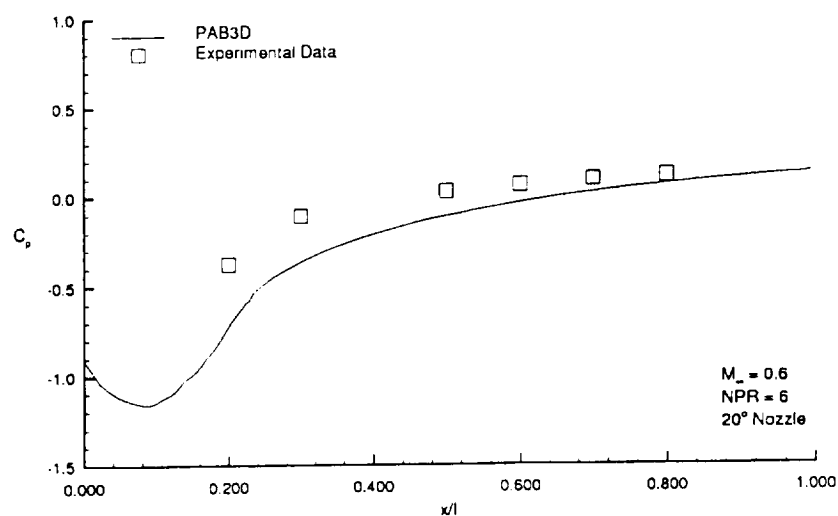
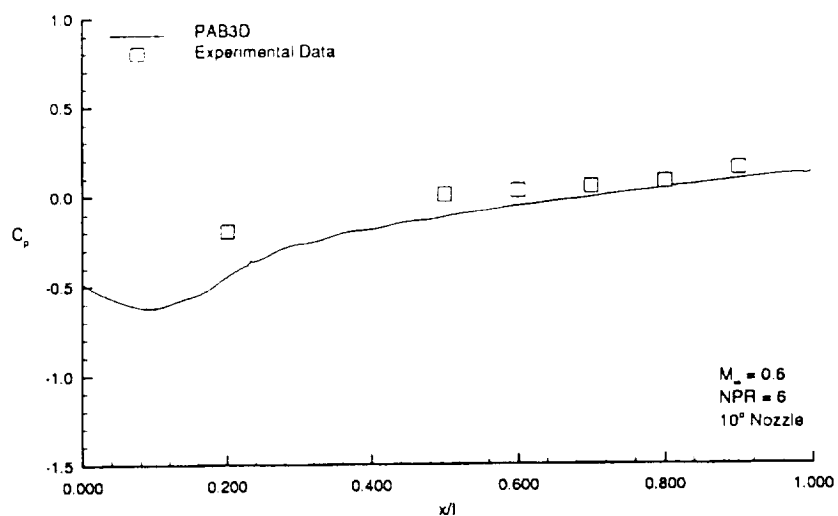


Figure 23: Comparison of Surface Pressure Distributions Between Afterbody
 Experimental Data and Baseline Computational Solutions: a) 10° , b) 20° , and c) 30°

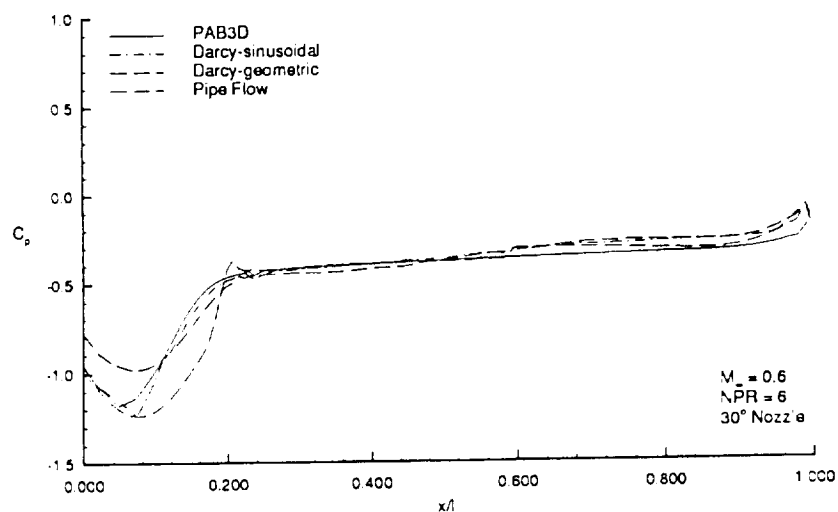
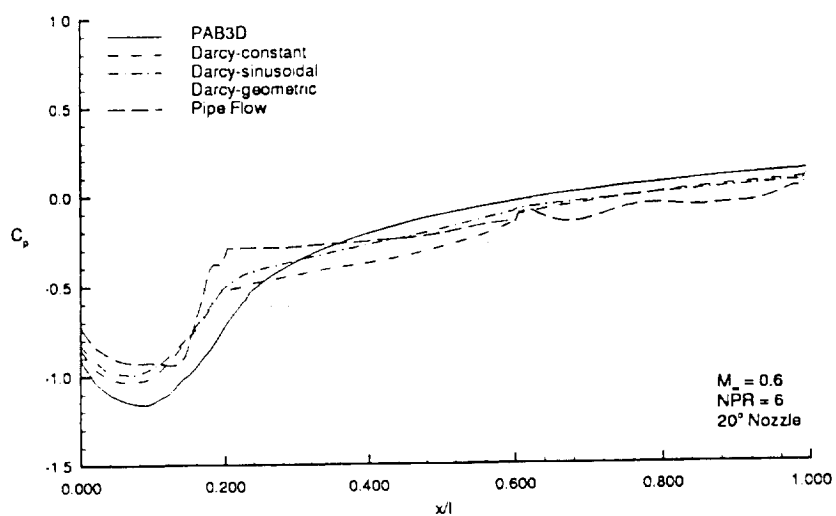
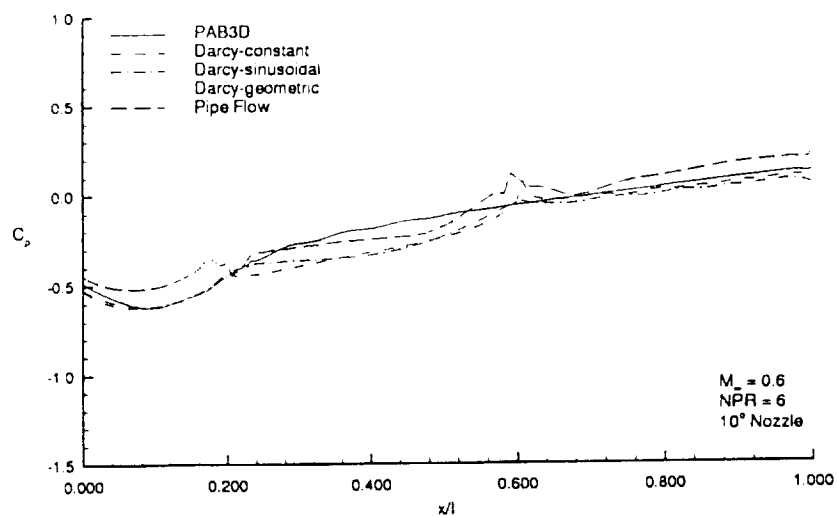


Figure 24: Comparison of Surface Pressure Distributions Between Baseline and Porous Afterbody Computational Solutions: a) 10°, b) 20°, and c) 30°

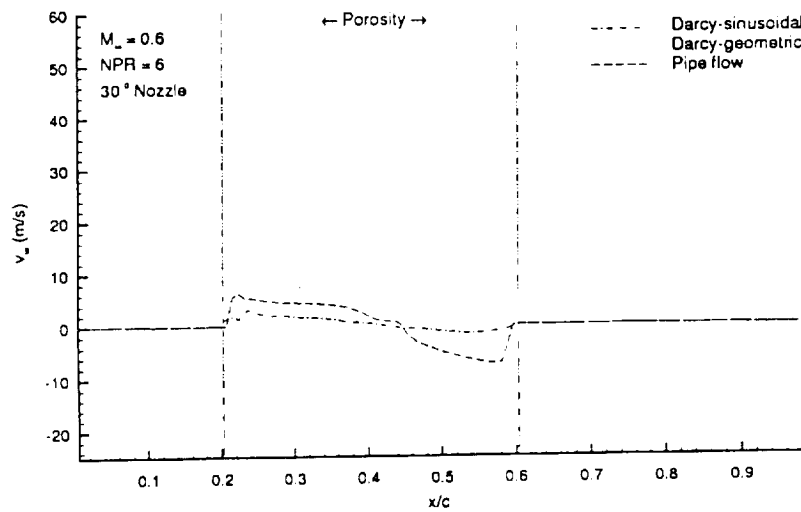
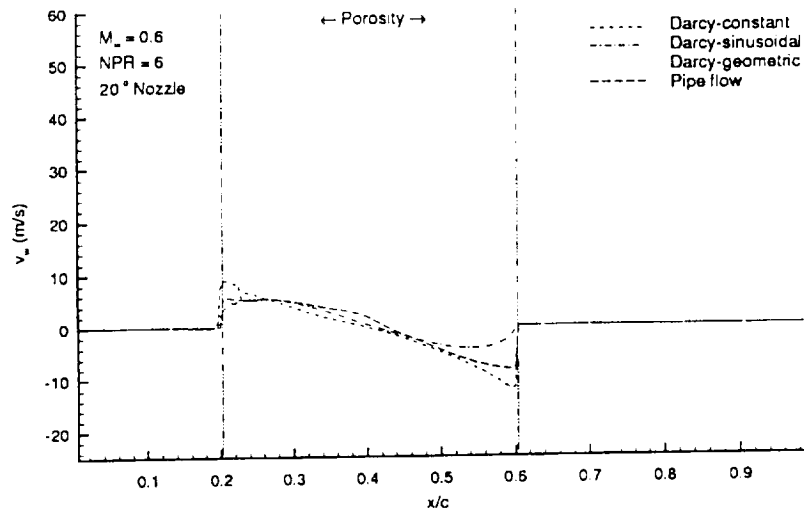
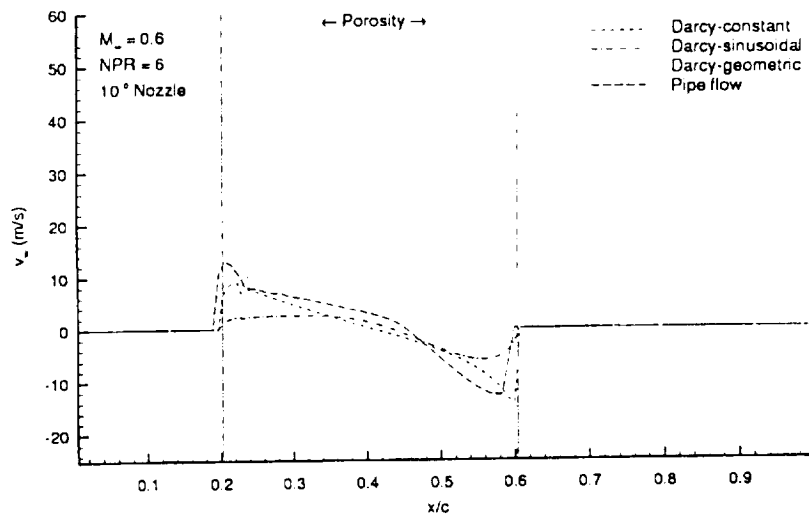


Figure 25: Comparison of Transpiration Velocity Distributions for Porous Afterbody Computational Solutions: a) 10°, b) 20°, and c) 30°

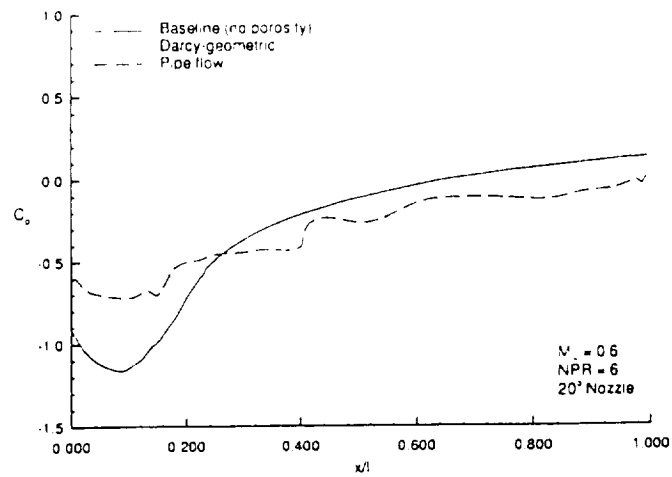


Figure 26: Surface Pressure Distribution for 20° Nozzle with Passive Control From 0%-40% of the Nozzle Length

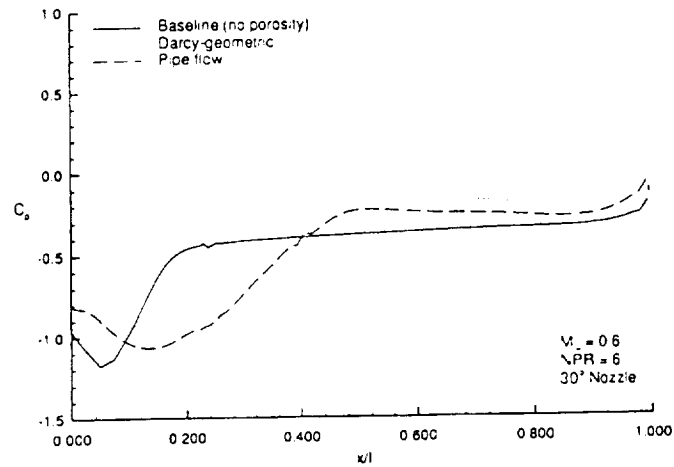


Figure 27: Surface Pressure Distribution for 30° Nozzle with Passive Control From 0%-40% of the Nozzle Length

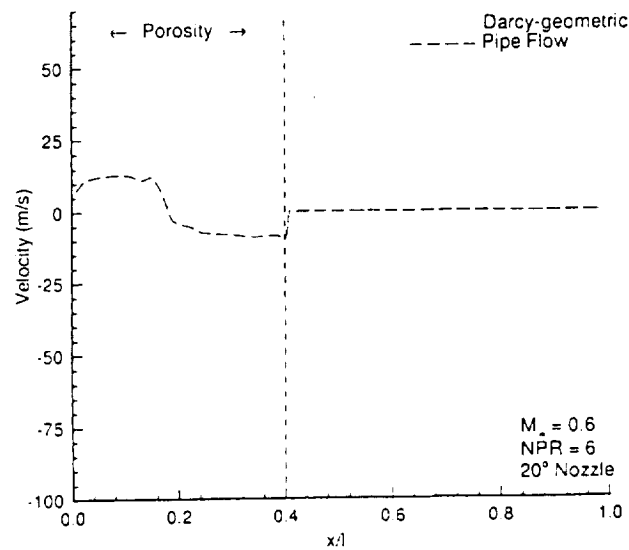


Figure 28: Transpiration Velocity Distribution for 20° Nozzle with Passive Control From 0%-40% of the Nozzle Length

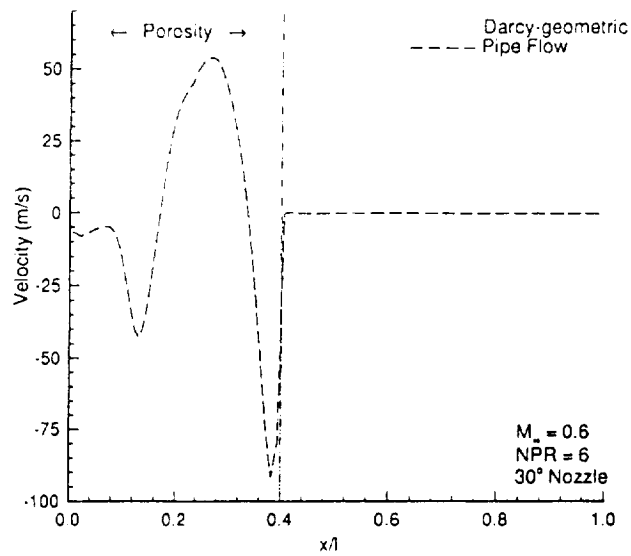


Figure 29: Transpiration Velocity Distribution for 30° Nozzle with Passive Control From 0%-40% of the Nozzle Length

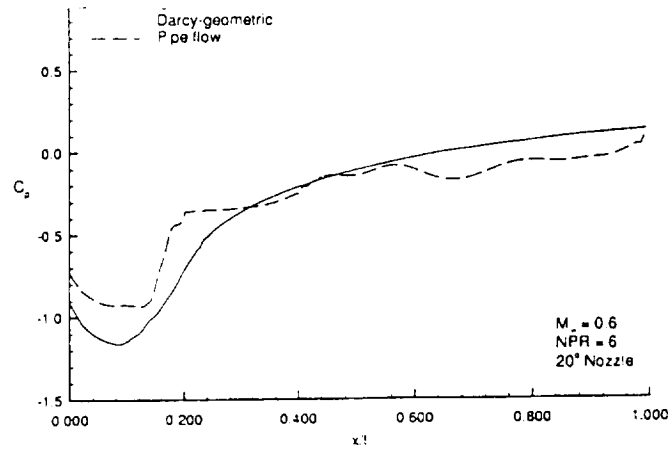


Figure 30: Surface Pressure Distribution for 20° Nozzle with Passive Control From 20%-40% of the Nozzle Length

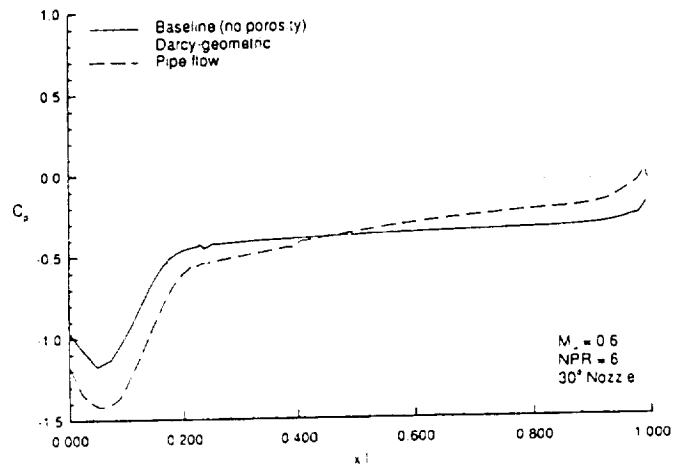


Figure 31: Surface Pressure Distribution for 30° Nozzle with Passive Control From 20%-40% of the Nozzle Length

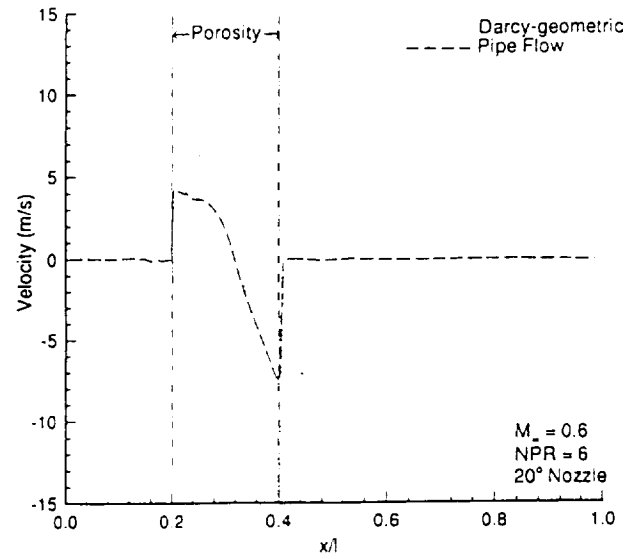


Figure 32: Transpiration Velocity Distribution for 20° Nozzle with Passive Control From 20%-40% of the Nozzle Length

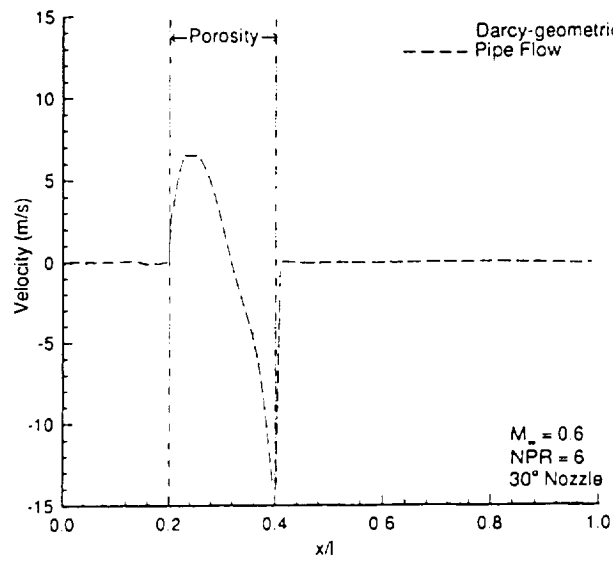


Figure 33: Transpiration Velocity Distribution for 30° Nozzle with Passive Control From 20%-40% of the Nozzle Length

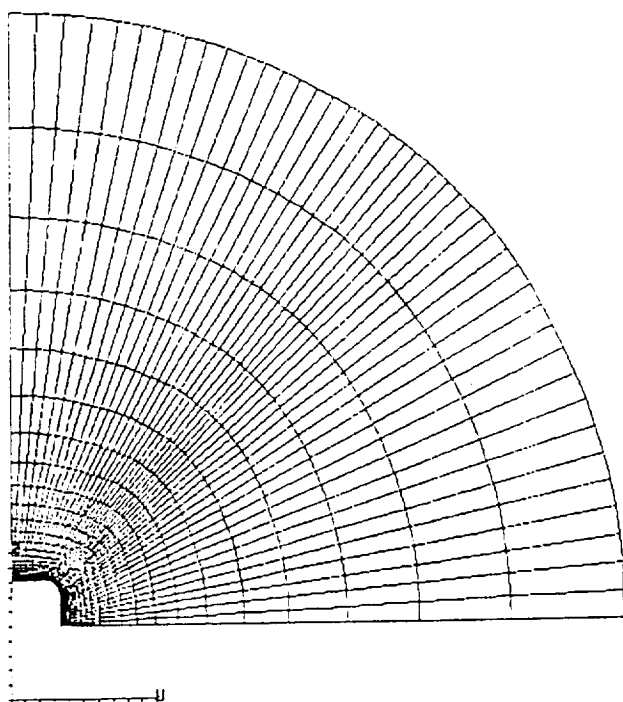
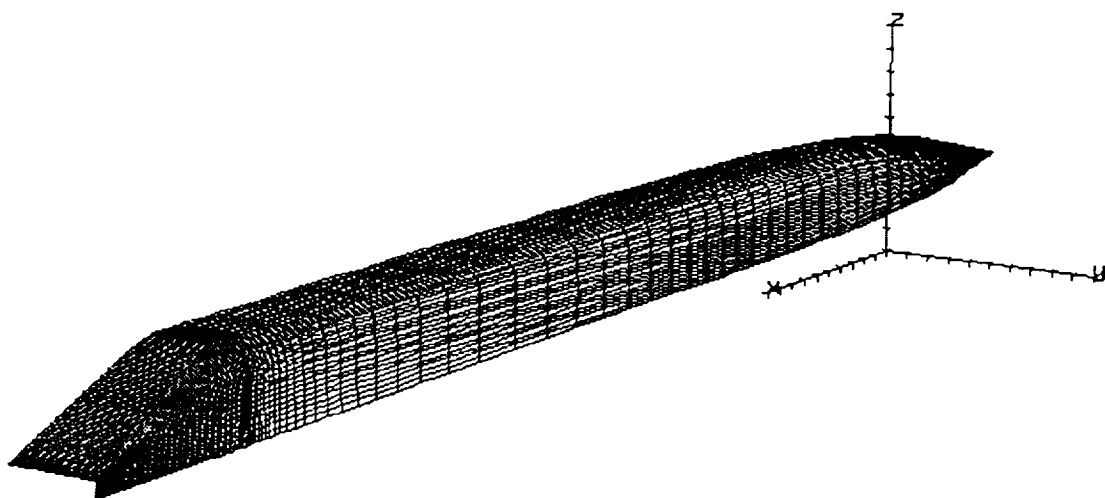


Figure 34: Three-Dimensional Afterbody Quarter Grid: a) Surface Grid. b) Cross-sectional View at Nozzle Connect

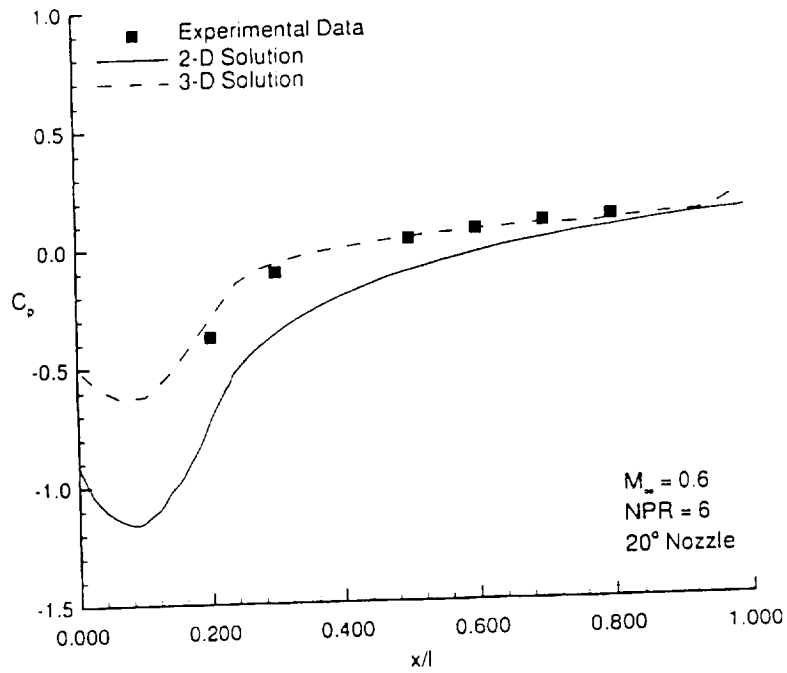


Figure 35: Comparison of Two- and Three-Dimensional Afterbody Solutions to Experimental Data for $M_\infty=0.6$

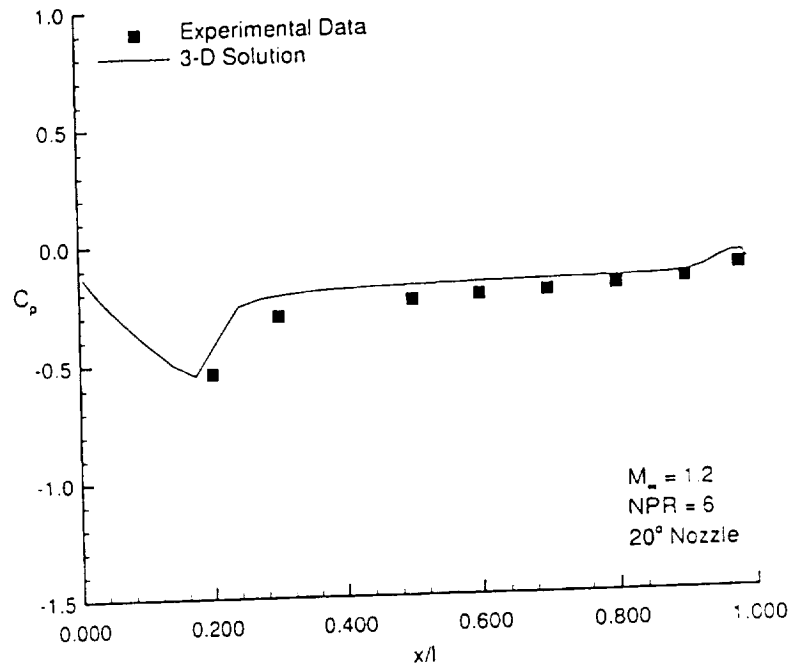


Figure 36: Comparison of Three-Dimensional Afterbody Solution to Experimental Data $M_\infty=1.2$